Detailed numerical simulations of primary atomization of airblasted liquid sheet

Anirudh Asuri Mukundan, Thibaut Ménard, Jorge César Brändle de Motta, Alain Berlemont

To cite this version:

Anirudh Asuri Mukundan, Thibaut Ménard, Jorge César Brändle de Motta, Alain Berlemont. Detailed numerical simulations of primary atomization of airblasted liquid sheet. International Journal of Multiphase Flow, 2022, 147, pp.103848. 10.1016/j.ijmultiphaseflow.2021.103848 . hal-03269139v2

HAL Id: hal-03269139

https://hal.science/hal-03269139v2

Submitted on 30 Nov 2021

Detailed numerical simulations of primary atomization of airblasted liquid sheet

Anirudh Asuri Mukundan[a,1], Thibaut Ménard[a,b,*], Jorge César Brändle de Motta[a,b], Alain Berlemont[a]

[a] *CNRS UMR6614 CORIA, Saint-Étienne-du-Rouvray, France*
[b] *Université de Rouen Normandie, Saint-Étienne-du-Rouvray, France*

Abstract

This paper investigates the primary atomization of airblasted liquid sheet using detailed numerical simulations. The atomization of liquid sheet under airblasting conditions involve complex mechanisms and a thorough understanding is necessary. A planar pre-filming airblast atomization configuration have been chosen to study the breakup of liquid sheet/film injected on a solid flat plate. We have investigated an operating point directly relevant for high altitude relight condition of the aircraft. This configuration has been chosen based on the experimental investigation of Gepperth et al [S. Gepperth, A. Müller, R. Koch, H.-J. Bauer, Ligament and droplet characteristics in pre-filming airblast atomization, Proceedings of the ICLASS, 12th Triennial International Conference on Liquid Atomization and Spray Systems, September 2-6, Heidelberg, Germany, 2012] for the airblast atomization. The numerical simulations have been performed using in-house Navier-Stokes solver that uses consistent mass and momentum flux computation technique. The purpose of this work is to provide a comprehensive database and analyses of the airblast atomization of liquid sheet. This include studies on the effect of velocity profile on the atomization characteristics, occurrence of secondary atomization and drop coalescence, and extraction of near-field atomization characteristics. The qualitative analyses of the results from the simulations showed that there are two major atomization mechanisms of liquid film breakup – sheet/bag breakup and ligament breakup. The drop diameter and velocity distributions computed from the simulations was found to be of the same order of magnitude although under-predicting the experimental data. Based on the atomized drop data, both the secondary atomization and drop coalescence have been observed to occur in the simulations. The quantitative analyses of the near-field liquid ligaments results revealed the lengths of these ligaments are of the same order of magnitude as the experimental data while an under-prediction in the ligament velocity has been observed. Finally, an excellent agreement between simulations and experimental data has been found for the Sauter Mean Diameter (SMD) of the atomized droplets.

Keywords: Primary atomization, Airblast atomization, Incompressible flows, Multiphase flows, Moment of Fluid method, Drop size distribution

---

1. Motivation and objectives

Air transport has been one of the fastest mode of transportation of passengers and freight between continents in the world. Despite the global COVID-19 pandemic, due to the stage-by-stage vaccine roll-out in many countries, it is predicted the aviation industry will soon bounce back. In fact, the pre-COVID estimates [1] show that the aviation industry has experienced a growth of about 2.5 times the number

---

[*] Corresponding author

Email addresses: `anirudh.mukundan@math.ubc.ca`, `anirudh.mukundan@coria.fr` (Anirudh Asuri Mukundan), `thibaut.menard@coria.fr` (Thibaut Ménard)

[1] current address: Department of Mathematics, University of British Columbia, Vancouver, Canada. *Contact Email address:* `anirudh.mukundan@math.ubc.ca`

Preprint submitted to International Journal of Multiphase Flow *September 17, 2021*

of passengers since the year 2000. Furthermore, Airbus [2] had a forecast of a 4.3% growth in the air traffic for the next 20 years. The Advisory Council for Aeronautics Research in Europe (ACARE), National Aeronautics Research and Development plan, and European Commission has put forth stringent regulations norms to meet by 2050 which include the norms on the pollutant emissions such as CO_2, NO_x and noise reduction [3, 4, 5]. With these regulations data on hand, it is imperative to design aero engines with high efficiency, low fuel consumption, and reduced pollutant emissions.

To that end, the lean combustion technologies (LCT) such as lean premixed prevaporized (LPP) combustion, Moderate or Intense Low-oxygen Dilution (MILD) combustion concepts are commonly employed in the gas turbines [6, 7]. In fact, the LCT is now a standard practice in reaching ultralow pollutant emissions by controlling the combustion temperature [8]. With the LPP and MILD combustion concepts, low temperature fuel combustion has become possible thereby reducing the NO_x, greenhouse gas, and unburnt hydrocarbons emissions. In order to extract the full efficiency from the lean combustion concept (LCC), it is imperative to have high quality of atomization/breakup of the injected liquid fuel. Moreover, this high quality of atomization has to be maintained at all operating conditions of the aircraft even at high altitude where the temperature can drop as low as $-50\,^{\circ}\mathrm{C}$. These objectives are met through a fuel injection technique involving airblasting condition of atomization of injected liquid fuel. Airblast atomization is the physical process in which low speed liquid fuel stream is sheared by high speed air (i.e., gas) stream leading to breakup into liquid drops and ligaments. In fact, a planar pre-filming type of airblast atomization involves thin film of liquid fuel injected on a solid flat plate which is destabilized into varying sized drops by the high speed air (about 100 times faster than fuel [9]) flowing above and below the plate. There are numerous breakup mechanisms involved in the pre-filming airblast atomization process. Hence, in order to control the fuel atomization, an improved understanding of this process is necessary.

Since the introduction of the concept of airblast atomization by Lefebvre and Miller [10], there have been numerous investigations of two configurations of airblast atomization – cylindrical and planar configurations. In the former, the liquid and gas are injected in a co-flowing setup in which the destabilization of the liquid jet by the high speed gas causes the atomization into droplets. In the latter, a thin liquid film is injected on a flat plate which is then destabilized into droplets by the high speed gas stream flowing above and below the plate.

On one hand, Lasheras et al. [11], Villermaux [12], Marmottant and Villermaux [13] performed extensive investigations to understand the breakup physics of the cylindrical airblast atomization configuration. These studies found that the liquid/gas interface is first subjected to Kelvin-Helmholtz (KH) instability due to momentum and velocity difference between the liquid and gas phases. The KH instability results in the surface waves on the liquid/gas interface which then forms bulges on the surface. These bulged portion of the interface are stretched into ligaments due to the high speed co-flowing air due to Rayleigh-Taylor (RT) type instability. These ligaments then subsequently breakup into droplets due to the capillary effect from the Rayleigh-Plateau (RP) instability. Apart from the experimental investigations, there have been attempts to numerically simulate the atomization for this cylindrical configuration. For example, Chiodi et al. [14], Chiodi and Desjardins [15, 16] were able to reproduce the breakup physics through numerical simulations using geometric liquid volume fraction transport method [17] and conservative level set method [18].

On the other hand, the planar configuration of airblast atomization has different breakup physics compared to its cylindrical counterpart. Many experimental [9, 19, 20, 21] and numerical [22, 23, 24, 25] works have investigated this configuration to understand the breakup physics and the atomization characteristics such as drop size distribution (DSD) and drop velocity distributions (DVD). Many of the past experimental studies have found that the aerodynamic forces play a significant and key role in the droplet sizes; specifically, the increase in the mean air velocities resulted in reduction in the droplet sizes [26, 27, 28, 29] while a reduction in the Sauter Mean Diameter (SMD) has been observed with the increase in the surface tension of the liquid fuel [26, 27]. A recent study by Chaussonnet et al. [30] investigated the influence of the ambient pressure, film loading, and gas velocity on the characteristics of the primary atomization of this pre-filming airblast atomization configuration and derived a novel connection between the pressure and the atomization quantities such as SMD, ligament lengths, and velocity through a scaling law. Multiple works using numerical simulations have been performed in the past years, for example, Fuster et al. [31] studied the instability frequency of the primary break up of planar coflowing sheets of water and air at dynamic pressure ratios of 0.5 to 32. Recently, Agbaglah et al. [32] studied the destabilization of the air/water planar liquid sheet and found an excellent agreement between experiments and simulations for liquid cone length, spatial growth of primary instability, and maximum wave frequency. The investigations by Bilger and Cant [23] performed simulations of planar airblast atomization with a laminar inlet velocity profile for the gas phase and developed a regime diagram for the atomization process using the liquid and gas phase velocities as the abscissa and ordinate, respectively.

Although there have been many numerical studies carried out in the past, they have predominantly focused on an operating condition that are not directly relevant to an aircraft engine operating condition. Since the products of liquid atomization are different for different operating conditions, Gepperth et al. [9] performed experimental investigation of planar pre-filming airblast configuration using Shellsol D70 (surrogate of Jet A-1 fuel) under various operating conditions. Of these operating conditions, the aircraft altitude relight condition has been of highlighted interest in their work. In fact, their study extracted near-field ligament breakup length and velocity data and far-field drop characteristics for variety of velocities of the gas stream. These characteristics are relevant because the airblast atomization thrives on the gas phase velocity and the momentum flux ratio ($q = \rho_{\mathrm{liq}} u_{\mathrm{liq}}^2 / \rho_{\mathrm{gas}} u_{\mathrm{gas}}^2$). Furthermore, there have been multiple experimental investigations [33, 34, 35] as well as numerical studies using large eddy simulations (LES) [36, 37, 25] for this planar airblast atomization configuration; embedded direct numerical simulations (eDNS) [38, 39, 40, 22] in which the DNS have been performed in a small domain embedded inside larger LES domain. Recently, Warncke et al. [22] used a diffused interface VOF method using OpenFOAM framework for simulating the primary atomization of a planar pre-filming airblast atomizing liquid sheet using eDNS approach. A satisfactory agreement in the results between the simulations and experiments have been found from their study. However, the limitations to the diffused interface method has been profoundly observed in the computation of the statistics of the droplet data. A recent work by Braun et al. [41] used meshless smoothed particle hydrodynamics (SPH) for numerically predicting the air-assisted atomization and compared their results with the work of Gepperth et al. [9]. Following this, Holz et al. [42] accurately simulated a 2D configuration of the airblast atomization at elevated pressures and extracted near-field quantities related to drop diameter, velocity, and trajectory as well as atomized liquid ligaments.

Although there have been several studies in the past that performed the numerical explorations and investigations into airblast atomization, the effect of inlet velocity profile on the atomization characteristics, droplet breakup mechanisms, and on the ligament breakup lengths and velocities are still missing links. This work is performed to improve the understanding of these links through detailed numerical simulations. Therefore, the objectives in this work are to:

- understand and identify predominant physical breakup mechanisms of airblast atomization,
- investigate the atomization characteristics such as drop size and velocity distributions,
- find the presence of secondary atomization and coalescence of drops in the computational domain,
- find the effect of liquid and gas inlet velocity profile on the atomization characteristics, and
- extract near-field data about ligament breakup lengths and velocities as well as breakup frequency.

To that end, a practically relevant and a computationally less expensive operating point of altitude relight condition is chosen for the investigation. The key practical difficulty in this operating point is the ignition and stabilisation of the fuel-air mixture when the aircraft is at high altitude of 11,000 m ($\approx 36,000$ feet) where the temperature of the air can go as low as $-50\,^{\circ}\mathrm{C}$.

This paper is organized as follows. Section 2 presents the details about the experimental investigations whose data are compared later with the results from the simulations performed in this work. Furthermore, this section presents the chosen computational domain along with the operating conditions for which the numerical simulations are performed. Then, the configuration, case setup, initial and boundary conditions, and numerical methods for the flow solver are presented in Section 3. Finally, the results from the numerical simulations are presented in Section 4 that include detailed qualitative and quantitative analyses of the breakup mechanisms, atomized droplets, and liquid ligaments.

2. Investigation domain and operating conditions

The simulations for the primary atomization of airblasted liquid sheet presented in this work are performed for a reduced geometry of an annular aircraft engine combustor similar to the experimental work of Gepperth et al. [9] and numerical work of Warncke et al. [22]. The rationale behind the reduction of the complex combustor geometry is to be able to perform detailed numerical simulations of primary atomization zone at a modest computational cost. The following subsections present the details of the configuration and operating conditions employed in the experimental investigation [9] and the numerical simulations performed in this work.

2.1. Experimental study

The experiments have been conducted at the spray test rig at the Institut für Thermische Strömungsmaschinen (ITS) in the Karlsruher Institut für Technologie (KIT). The test section of the experiment [9] is a two-dimensional abstraction (i.e., reduced geometry) of an annular combustor consisting of four wall segments and pre-filming flat plate upon which the liquid fuel is injected as a thin film/sheet. This film is then destabilized by the high speed air flowing above and below it. The air from the mixer have been split into two streams such that each stream flows above and below the pre-filmer plate. The liquid is continuously fed on the pre-filmer plate through a set of 50 equidistant distributed holes each with a diameter of 0.5 mm. The liquid flow through the test section have been controlled by a mass flow meter/controller.

The primary breakup process and the flow of the liquid film has been obtained through high speed shadowgraphy technique. A set of two high speed video cameras of 7 kHz at a spatial resolution of 13.89 µm with a field of view of approximately 14.2 mm × 14.2 mm have been used. The cameras have been placed at a 90° shift so that both the side and the top view of the film disintegration can be captured. The exposure time has been reduced to 1 µs minimizing the blurring effect of the fast deforming liquid structures and droplets. The measurement volume have been illuminated using two 500 W halogen spotlights mounted opposite to the cameras. Then, a double image (each shifted spatially by 90°) has been recorded every 3 s over a total time of 30 s with the rationale that each recorded droplet must have left the field of view within 3 s. Each drop found in the double image has been considered for the purpose of statistical analysis such as computation of probability density function (PDF) of drop size distribution (DSD) and drop velocity distribution (DVD). In addition to the far-field droplets, the near-field liquid ligaments are captured in the shadowgraphy images from the accumulated liquid in the trailing edge of the pre-filmer plate as shown in Figure 1. The technique of ligament tracking velocimetry [43], has been employed to distinguish the droplet liquid structure from ligament liquid structure in the images. This technique is based on on back light illumination (i.e., shadowgraphy) with a double-pulsed laser. The field of view is 12 mm × 16 mm with a spatial resolution of 10 µm. The main advantage of this measurement technique is that the details about the drops and the accumulated liquid shown in Figure 1 are obtained simultaneously. A total of 38,000 drops and 13,000 liquid ligaments have been recorded from the shadowgraphy images.

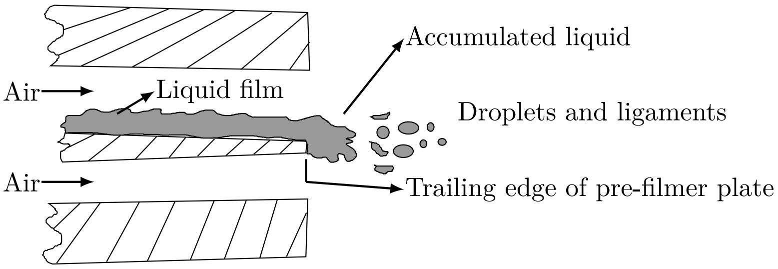

Figure 1: Illustration of instability waves on liquid film, liquid accumulation at pre-filmer plate edge, as well as droplet and ligament formation.

Robust statistical results have been derived from the obtained experimental images using an efficient algorithm [44] which has been extended by a depth of field (DoF) correction to further increase the measurement accuracy. It is to be remarked that, within the context of this algorithm, the drops need not be spherical to be able to measure its diameter and velocity. The post-processing algorithm for the images developed at the ITS [45, 44, 46] can be divided into four parts. First, a gray scale image is obtained from each experimental raw image using a threshold value based on pixel intensity distribution. Second, connected structures are identified using a contour tracking algorithm which further divides the area into drops and accumulated liquid (from which the liquid ligaments are disintegrated). Third, in order to compute the droplet velocities, a first estimation is obtained from the particle image velocimetry (PIV). This is employed as a "first guess" to a least-square fitting algorithm to calculate the final velocity using the drop displacement and the inter-frame timing obtained from the double image. And, finally, geometrical parameters of the accumulated liquid such as length and velocity of liquid ligaments are computed.

The uncertainties in the experimental measurements have been determined using the approach described by Kline and McClintock [47]. These uncertainty values are measured to be 3% for air velocity, 0.5% for liquid mass flow, 4% for measurement of drop size and velocity summing upto a an approximate 7%. For more detailed information about the experimental setup and post-processing procedure, the reader is referred to Refs. [9, 22, 45, 43, 44].

2.2. Numerical simulations

A planar pre-filming configuration is considered in this work for detailed numerical simulations of primary atomization of airblasted liquid sheet. This configuration, as shown in Figure 2, is a geometry simplification (c.f. Figure 2b) of the annular atomizer (c.f. Figure 2a). In this simplified geometry, liquid fuel is injected as a thin film on a solid pre-filmer plate which is then destabilized by the high speed air flowing above the liquid inlet and below the pre-filmer plate. It is to be remarked that the length of the computational domain along the downstream direction in this work is 10% longer than that of the work of Warncke et al. [22]. The rationale behind having a longer downstream length of the computational domain is to accurately capture the characteristics and physics of atomization of liquid droplets. The dimensions of the computational domain, pre-filmer plate and the height of the liquid fuel film used in the simulations (c.f. Figure 3a) along with the boundary conditions (c.f. Figure 3b) are marked in Figure 3 whose values are given in Table 1. The chosen length of the pre-filmer plate l_{pf} measured 1 mm is smaller than the experimental setup [9]. It was found [9] that changes to this length have no significant impact on the atomization process and therefore is sufficient to reproduce the liquid film breakup. A boundary layer of gas on the liquid with thickness $\theta = 25.78\,\mu\mathrm{m}(= 2\Delta x)$ is employed to take into effect the instability wave formation on the liquid phase due to high shear from the gas phase and the avoid the sudden jump in the velocity between liquid and gas phases.

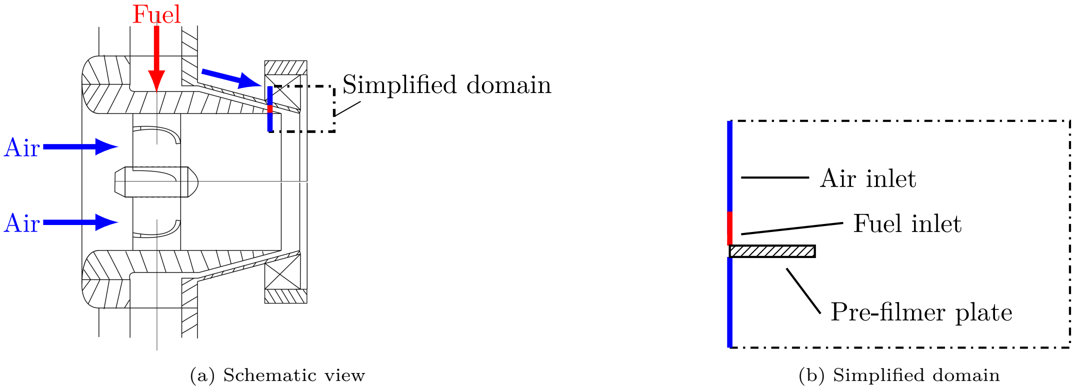

(a) Schematic view

(b) Simplified domain

Figure 2: Schematic view of the planar pre-filming airblast atomizer and simplified computational domain for numerical simulations.

The fuel and the air are injected from the $z+$ plane under an inflow boundary condition with $z-$ being outflow boundary condition, periodic boundary conditions are imposed along the y direction (to mimic the larger flat pre-filmer plate configuration like used in the experiments [9]), and outflow boundary conditions

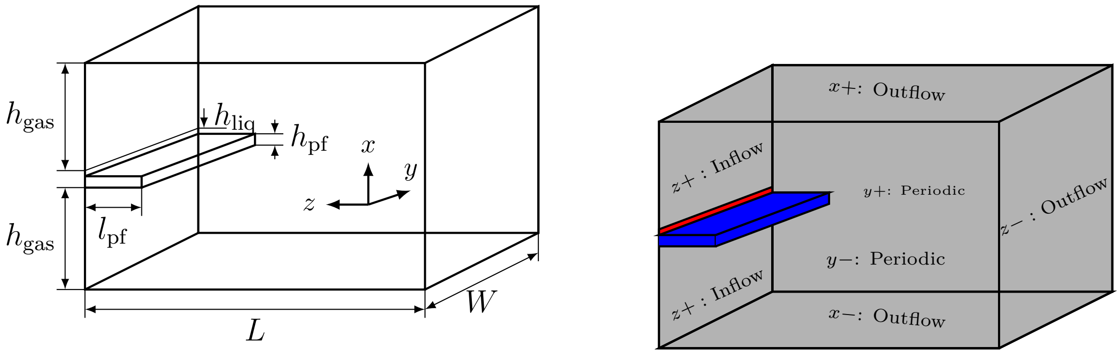

(a) Dimension of simulation domain

(b) Boundary conditions

Figure 3: Dimensions and boundary conditions used in the computational domain with red region representing fuel inlet and blue region depicting solid pre-filmer plate.

Table 1: Dimensions of computational domain.

L	W	h_{gas}	h_{liq}	l_{pf}	h_{pf}
6.6 mm	3.3 mm	1.5 mm	100 µm	1 mm	200 mm

are imposed on the remaining planes of the computational domain are imposed. The details of the boundary condition for each face of the computational domain is given in Table 2.

Table 2: Summary of boundary condition for each face of the computational domain.

Coordinate direction	**Face**	**Boundary condition**
$x+$	Top face	Outflow
$x-$	Bottom face	Outflow
$y+$	Rear face	Periodic
$y-$	Front face	Periodic
$z+$	Left face	Inflow
$z-$	Right face	Outflow

2.3. Operating conditions

The parameters of the altitude relight operating condition [48, 49] employed in this work for the detailed numerical simulations are summarized in Table 3 where w_{liq} is the velocity of liquid, w_{gas} is the velocity of gas, ρ is the density, ν is the kinematic viscosity, σ is the surface tension, $\Lambda_{\mathrm{liq.film}}$ is the 2D volumetric liquid film loading, r_ρ is the density ratio, r_ν is the kinematic viscosity ratio, q is the momentum flux ratio, Re is the Reynolds number, We is the Weber number, and $h_{\mathrm{chw}} = 4\,\mathrm{mm}$ is the half channel width of the injection channel in the annular combustor. It is to be remarked that in order to be consistent with respect to the experimental conditions, the 2D volumetric liquid film loading $\Lambda_{\mathrm{liq.film}}$ is computed as the ratio of liquid mass flow rate and width of the pre-filmer plate employed in the experiments [22]. The expressions for the non-dimensional numbers listed in this table are defined in Table 4.

The liquid fuel Shellsol D70 is used in the simulations for two reasons: first, its physical properties (specifically, viscosity μ and surface tension σ) at ambient temperature are similar to the Jet A-1 fuel and second, its low surface tension (thereby promoting droplet breakup) that will be useful for its use in the simulations of primary atomization. Moreover, the experimental study [9] has employed Shellsol D70, hence, it will be beneficial to compare the results from the simulation with the experiments for the same fuel properties. Hence, having a smaller computational domain coupled with low surface tension will be beneficial to observe large number of physical atomization events.

Table 3: Summary of Operating Conditions.

Parameter	**SI Unit**	**Value**
Liquid Properties		
w_{liq}	m/s	0.5
ρ_{liq}	kg/m^3	770
ν_{liq}	m^2/s	2.03×10^{-6}
σ	kg/s^2	2.75×10^{-2}
$\Lambda_{\mathrm{liq.film}}$	mm^2/s	50
Gas properties		
w_{gas}	m/s	50
ρ_{gas}	kg/m^3	1.2
ν_{gas}	m^2/s	1.5×10^{-5}
Non-dimensional numbers		
$\mathrm{Re}_{\mathrm{gas}}$	[-]	13,333
$\mathrm{Re}_{\mathrm{liq}}$	[-]	24.63
We	[-]	21.38
q	[-]	15.58
r_ρ	[-]	641.67
r_ν	[-]	13.6

Table 4: Expressions for non-dimensional numbers characterizing the flow.

$\mathrm{Re}_{\mathrm{liq}} = \Lambda_{\mathrm{liq.film}}/\nu_{\mathrm{liq}}$	$\mathrm{Re}_{\mathrm{gas}} = w_{\mathrm{gas}} h_{\mathrm{chw}}/\nu_{\mathrm{gas}}$	$\mathrm{We} = \rho_{\mathrm{gas}}(w_{\mathrm{gas}} - w_{\mathrm{liq}})^2 h_{\mathrm{pf}}/\sigma$
$q = \rho_{\mathrm{liq}} w_{\mathrm{liq}}^2/\rho_{\mathrm{gas}} w_{\mathrm{gas}}^2$	$r_\rho = \rho_{\mathrm{liq}}/\rho_{\mathrm{gas}}$	$r_\nu = \nu_{\mathrm{liq}}/\nu_{\mathrm{gas}}$

The liquid and gas Reynolds numbers are computed following the work of Chaussonnet et al. [50]. The Weber number is computed based on the gas phase density, liquid and gas slip velocity, and thickness of the pre-filmer plate due to the significance of the impact on the ligament breakup length observed by Gepperth et al. [9]. In fact, the Reynolds and Weber number in the flows inside aircraft engines are very high leading to a highly turbulent flow condition. Such high turbulence often produce very small liquid structures which require high mesh resolution to be captured by a fixed grid interface reconstruction methods. Hence, in order to be computationally efficient to simulate the primary atomization of airblast liquid sheet, we have comparatively reduced the Reynolds and Weber number with respect to the real-time aircraft engines.

3. Numerical setup

3.1. Incompressible Navier–Stokes equations

The incompressible multiphase flows can be described by the following set of conservative form of the Navier-Stokes equations

$$\boldsymbol{\nabla} \cdot \boldsymbol{u} = 0, \tag{1}$$

$$\frac{\partial \rho \boldsymbol{u}}{\partial t} + \boldsymbol{\nabla} \cdot (\rho \boldsymbol{u} \otimes \boldsymbol{u}) = -\boldsymbol{\nabla} P + \boldsymbol{\nabla} \cdot (2\mu \boldsymbol{D}) + \boldsymbol{B}, \tag{2}$$

where $\boldsymbol{u}$ is the velocity field, ρ is the density, μ is the dynamic viscosity, P is the pressure field, $\boldsymbol{D}$ is the strain rate tensor given as $\boldsymbol{D} = \frac{1}{2}(\boldsymbol{\nabla}\boldsymbol{u} + (\boldsymbol{\nabla}\boldsymbol{u})^T)$, and $\boldsymbol{B}$ is the sum of the body and surface tension forces.

$\boldsymbol{B} = \boldsymbol{B}_\mathrm{b} + \boldsymbol{B}_\mathrm{st}$ where $\boldsymbol{B}_\mathrm{b}$ is the force due to gravity (neglected in this work) and $\boldsymbol{B}_\mathrm{st}$ is the force due to surface tension which is given as $\boldsymbol{B}_\mathrm{st} = \sigma\kappa\delta_I\boldsymbol{n}$. σ represent the surface tension, κ is the curvature of the interface computed using the level set function ϕ according to

$$\kappa(\phi) = -\boldsymbol{\nabla} \cdot \left(\frac{\boldsymbol{\nabla}\phi}{\|\boldsymbol{\nabla}\phi\|_2} \right), \tag{3}$$

and δ_I is the Dirac delta function centered on surface of the interface.

Within the context of two-phase flows, an interface $\mathit{\Gamma}$ separates the liquid and the gas phase. The material properties such as density and viscosity are assumed to be constant within each phase, i.e., $\rho = \rho_\mathrm{liq}$ and $\mu = \mu_\mathrm{liq}$ in liquid phase and $\rho = \rho_\mathrm{gas}$ and $\mu = \mu_\mathrm{gas}$ in gaseous phase. However, these properties are subject to a jump at the location of the liquid/gas interface. This jump is written as $[\rho]_\mathit{\Gamma} = \rho_\mathrm{liq} - \rho_\mathrm{gas}$ and $[\mu]_\mathit{\Gamma} = \mu_\mathrm{liq} - \mu_\mathrm{gas}$ while the velocity field remains continuous across the interface, hence $[\boldsymbol{u}]_\mathit{\Gamma} = 0$. However, the pressure is not continuous across the interface and it is possible to write the pressure jump [51] across the interface as

$$[P]_\mathit{\Gamma} = \sigma\kappa(\phi) + 2[\mu]_\mathit{\Gamma}(\nabla\boldsymbol{u} \cdot \boldsymbol{n}) \cdot \boldsymbol{n}, \tag{4}$$

where $\boldsymbol{n}$ is the unit normal of the liquid/gas interface pointing towards the liquid phase in a computational cell.

3.2. Flow solver

To simulate the primary atomization of airblasted liquid sheet, we use in-house Navier-Stokes equation solver ARCHER [52] in this work. The capabilities of ARCHER have been presented in many of the previous works [53, 54, 55, 56]. This solver is structured, parallel, and developed for direct numerical simulations (DNS) of complex and turbulent multiphase flows with the application to study primary atomization of liquid jet. The liquid/gas interface is represented by level set contiguous signed distance function and the mass conservation in the computational domain is ensured using volume fraction (see Section 3.3 for more details). This solver has been validated for various cases of complex turbulent flow configurations [57, 58, 59] thus, the numerical methods employed in this solver are tailored for treating turbulence in the system.

A staggered grid configuration is used with central finite difference scheme for least numerical dissipation. The scalar variables such as liquid volume fraction, density, viscosity, level set function, and pressure are stored in the cell center while the vector variables such as components of velocity and vorticity are stored in cell faces. A consistent mass and momentum flux computation [53] technique is employed in the solver that facilitates to perform simulations of large density ratio between liquid and gas phases.

A second-order central difference scheme is employed for discretization of the spatial derivatives to avoid any dissipation. However, the convection term is discretized using fifth-order WENO scheme to ensure a robust behavior of the solution. A semi-implicit formulation proposed by Sussman et al. [60] is used for discretizing the viscous term yielding second-order accuracy in regions away from the liquid/gas interface and first-order accuracy near the interface. The ghost fluid method (GFM) [61] is employed for the spatial discretization of the Poisson equation for taking into account the force due to surface tension as a pressure jump. The resulting linear system of symmetric and positive definite matrix with five diagonals is solved using multigrid algorithm for preconditioning a conjugate gradient (CG) method [62]. A projection method with a predictor-corrector time integration scheme is used to solve the Navier-Stokes equation with the time step size Δt determined based on the Courant-Friedrichs-Lewy (CFL) condition. The reader is referred to Ref. [53] for more details on the implementation of the numerical methods, schemes, and solution algorithm employed in the ARCHER solver.

The shape and walls of the solid pre-filmer plate are reproduced using staircase immersed boundary method (SIBM) similar to that described by Vu [63]. The SIBM is a form of the immersed boundary method (IBM) approximates the shape of the boundary such that it falls onto the Cartesian grid lines. The walls of the pre-filmer plate are treated as non-wetting walls used in the boundary condition of the liquid film injected on the plate. It is to be remarked that no solid-liquid wetting model is used for the liquid film injection on the plate in ARCHER solver. The representation of the walls of this pre-filmer plate by the SIBM technique is depicted in Figure 4. The contact angle between the liquid and solid is kept to 90°.

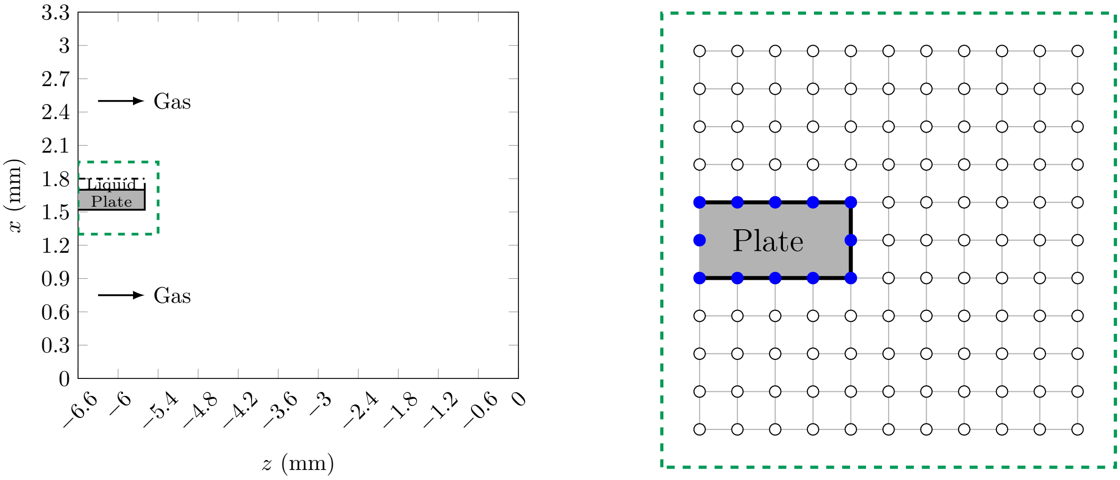

Figure 4: Illustration of solid pre-filmer plate representation (left figure) using staircase immersed boundary method (SIBM) with a zoomed view of pre-filmer plate region (right figure). The blue filled circles in the right figure represent the grid points on the surface of pre-filmer plate and white unfilled circles represent the grid points in the rest of the computational domain.

A turbulent velocity profile is imposed at the inlet $z+$ plane (c.f. Figure 3b) for the liquid and gas phases. The turbulence in the simulations is initiated in the gas phase using synthetic turbulence method [64]. The turbulent fluctuations in the velocity of the gas phase w'_{gas} is set to 10% of the bulk gas velocity w_{gas} at the plane of gas injection, i.e., $w'_{\text{gas}} = 0.1 w_{\text{gas}}$. The turbulent integral length scale is set to 3% of the total gas channel height h_{gas}, i.e., $l_t = 0.03 \times (2h_{\text{gas}})$. With the injected velocity flucutations and the chosen turbulent length scale, the turbulent Reynolds number is determined to be $Re_\tau = u' l_t / \nu_{\text{gas}} \approx 80$. Based on the relation $\eta / l_t \sim (Re_\tau)^{-3/4}$ [65] for single phase constant density and constant viscosity flows, we get the Kolmogorov length scale in the gas phase to be $\eta \approx 3.36\,\mu\text{m}$. Hence, according to Equation 9.6 in Pope [65], the relation between the required minimum mesh spacing and the Kolmogorov length scale is given as

$$\frac{\Delta x_{\min}}{\eta} \approx 2, \tag{5}$$

i.e., a mesh spacing about twice the size of the smallest eddy (Kolmogorov length scale) is required to fully resolve all scales of turbulent motion in a single phase flow. However, this work deals with two-phase flows in which the liquid/gas interface is assumed to be of infinitesimal thickness. This means that the scales of motion are considered well resolved at the limit of the infinitesimal interfacial thickness which is challenging to achieve for two-phase flows simulations [66] with our available computational resources [67]. Nevertheless, this relation could be considered to give an estimated value of the required minimum mesh spacing based on the Kolmogorov length scale.

3.3. Numerical method

Within the context of two-phase flows, it is imperative to track the location of the liquid/gas interface to accurately capture the flow physics. In order to accurately capture and track this interface, we use a hybrid moment of fluid–level set (HyMOFLS) method [68, 69]. The HyMOFLS interface reconstruction method uses moment of fluid (MOF) method [52] and the level set (LS) framework from the coupled level set volume of fluid (CLSVOF) method [51]. A piecewise linear interface calculation (PLIC) technique is employed in this method in which the interface is reconstructed as three dimensional planes. The methodology involved in the HyMOFLS method is described in the following subsections.

3.3.1. Moment of fluid (MOF) method

As mentioned above, the HyMOFLS is an amalgamation of the MOF and LS (from the CLSVOF method) frameworks of interface reconstruction. In this subsection, we present the methodology and the algorithm involved in the MOF method of interface reconstruction. The moment of fluid (MOF) method [70, 71, 52] can be considered as a generalized VOF method because it uses liquid volume fraction F (zeroth moment of liquid volume) as well as centroid $\boldsymbol{x}_{\mathrm{COM}}$ of liquid phase (first moment of liquid volume) in each computational cell to reconstruct the liquid/gas interface. With the 3D planar representation of the interface from PLIC technique, the equation of the interface is $ax+by+cz+d=0$ with the unit normal of this interface determined to be $\boldsymbol{n}=[a,b,c]^T$. The position and orientation of the interface are governed by the parameters d and $\boldsymbol{n}$ respectively. The MOF method of interface reconstruction computes the accurate values of the parameters d (defining the position of the interface) and $\boldsymbol{n}$ (defining the orientation of the interface) through the solution to the following equations:

$$\left|F^{\mathrm{ref}} - F^{\mathrm{act}}(\boldsymbol{n},d)\right| = 0, \text{ and} \tag{6}$$

$$E^{\mathrm{MOF}}(\boldsymbol{n},d) = \left\|\boldsymbol{x}^{\mathrm{ref}}_{\mathrm{COM}} - \boldsymbol{x}^{\mathrm{act}}_{\mathrm{COM}}(\boldsymbol{n},d)\right\|_2 . \tag{7}$$

On one hand, the interface position d is determined by conserving the liquid (and gas) phase volume between the reference (original) and actual (reconstructed) interfaces as demonstrated by the solution of Equation (6) where F is the liquid volume fraction in a computational cell. The liquid volume fraction F is defined as the ratio of the volume of liquid to that of the computational cell and hence $F \in [0,1]$. The gas phase volume fraction can be determined in a straightforward manner as $F^{\mathrm{gas}} = 1 - F$. The phase based properties such as density ρ and viscosity μ are obtained according to $\alpha = \alpha_{\mathrm{liq}}F + \alpha_{\mathrm{gas}}(1-F)$ where $\alpha = [\rho,\mu]$. On the other hand, the accurate orientation of the interface $\boldsymbol{n}$ is determined by solving the Equation (7) in which the E^{MOF} represent the centroid defect. It is defined as the Eucledian distance between the reference and actual centroids of the reference and actual interfaces respectively. The idea of the MOF method is depicted in the Figure 5 for a two dimensional computational cell configuration with liquid phase centroids.

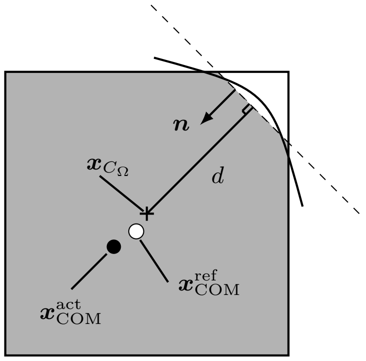

Figure 5: Exemplary computational cell in two dimensions with reference (original) and actual (reconstructed) liquid phase centroids. The reference interface is depicted as solid curved line and actual interface is depicted as dashed straight line.

The methodology of solving the Equations (6) and (7) involves first choosing a reference phase whose centroid is farthest from the computational cell centre. The rationale behind choosing the reference phase in this manner lies behind the fact that the phase with farthest centroid (i.e., phase with the least volume) has highest sensitivity towards the orientation of the liquid/gas interface. Next, an initial guess to the unit normal of the interface $\boldsymbol{n}$ is obtained from the level set function. Using this initial guess, the value of d is obtained by solving the Equation (6) such that volume is conserved under the reconstructed interface upto the machine precision. Then, the centroid defect E^{MOF} is minimized through Gauss-Newton iterative algorithm to obtain the optimal values for both d and $\boldsymbol{n}$. For detailed explanation, algorithms, and code implementations of the MOF method, the reader is referred to [52].

The advection of the interface within the framework of MOF method involves advection of liquid volume fraction as well as the liquid and gas phase centroids. The transport of liquid volume fraction is governed by

$$\frac{\partial F}{\partial t} + \boldsymbol{u} \cdot \boldsymbol{\nabla} F = 0, \tag{8}$$

solved using a directionally split advection algorithm [72]. The transport of the liquid and gas phase centroids is performed according to

$$\frac{\partial \boldsymbol{x}_{\mathrm{COM}}}{\partial t} = \boldsymbol{u}(\boldsymbol{x}_{\mathrm{COM}}), \tag{9}$$

where $\boldsymbol{u}(\boldsymbol{x}_{\mathrm{COM}})$ is the velocity at the location of the centroid $\boldsymbol{x}_{\mathrm{COM}}^{\mathrm{ref}}$ linearly interpolated from the cell face-centered velocity. The reader is referred to Appendix A of Ref. [70] for the detailed derivation of the Equation (9). This transport equation is solved using a directionally-split advection algorithm with an Eulerian Implicit–Lagrangian Explicit (EI–LE) scheme, more details can be found in Ref. [52].

3.3.2. Coupled level set volume of fluid (CLSVOF) method

The CLSVOF method employed in this work, within the context of HyMOFLS framework, follows the study of Ménard et al. [51]. In their study, the level set signed distance function ϕ defines the location of the interface the VOF method is used in conjunction to for the purpose of conservation of mass. Within the context of CLSVOF method, the parameters of the liquid/gas interface, i.e., d is determined by geometric method [73] and $\boldsymbol{n}$ is determined according to the methodology described by Ménard et al. [51]. The equation, methodology, and numerical method involved in transport of the level set function is performed the same was as for the liquid volume fraction (see Equation (8)). The coupling between the level and VOF method within the context of CLSVOF method involves the mutual correction of the values performed simultaneously conserving the liquid volume and the computation of the interface curvature is not affected. The implementation of the level set advection, correction and coupling with VOF method is performed similar to a classical CLSVOF method [74]; details of it are not recalled here.

3.3.3. Hybrid moment of fluid–level set (HyMOFLS) method

The MOF method is relatively more accurate than the CLSVOF method [52], however requiring higher computational cost [75]. In fact, it has been shown [52] that MOF method is accurate in capturing the interface in the under-resolved regions of the flow than the CLSVOF method. Therefore, the rationale behind the development of HyMOFLS framework [68] is to use MOF method for the interface reconstruction in the simulations only when it is necessary, i.e., in the under-resolved regions of the flow. Such regions are identified through the proposition of the parameter called interface resolution quality (IRQ) defined as

$$\mathrm{IRQ} = \frac{1}{\kappa \Delta x}, \tag{10}$$

where κ and Δx correspond to the local interface curvature and local mesh spacing respectively. The following criterion is checked in each computational call to choose between MOF and CLSVOF methods of interface reconstruction in it.

$$\mathrm{IRQ} = \frac{1}{\kappa \Delta x} = \begin{cases} < 2, \Rightarrow \text{Under-resolved structure} \Rightarrow \text{Use MOF method,} \\ \geq 2, \Rightarrow \text{Resolved liquid structure} \Rightarrow \text{Use CLSVOF method.} \end{cases} \tag{11}$$

In order to reduce the computational expense even further in the HyMOFLS method, this criterion is checked in the cells in the neighborhood of the interface as shown in Figure 6 where the solid line represent the liquid/gas interface, red cells correspond to the MOF method tagging, and the blue cells to the CLSVOF method tagging. As can be seen from this figure, the MOF method is tagged only in the cells with high curvature change (often a characteristic of under-resolved interfacial structures) while the CLSVOF method is tagged for the remainder regions.

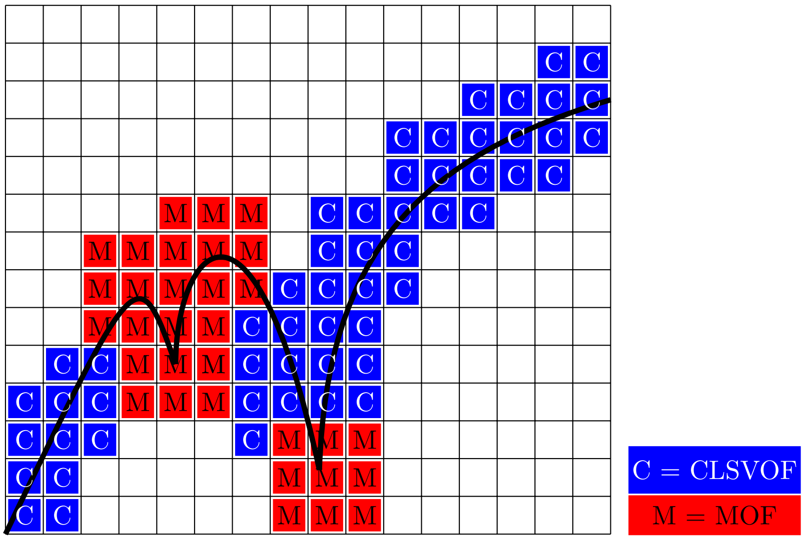

Figure 6: Narrow band of the MOF method tagged cells (red cells with value 1) and CLSVOF method tagged cells (blue cells with value 0) around the liquid/gas interface (shown in black solid line).

3.4. Simulation cases investigated

This paper aims to investigate the primary atomization of airblasted liquid sheet and extract the atomization characteristics. The specific focus of this work lies on the effect of inlet velocity profile (for the liquid and gas phases) on the atomization characteristics. To that end, we perform two sets of simulations imposing two different velocity profiles on the liquid and gas inlet – first, flat profile (Fp) (also called plug flow profile) for liquid phase and gas phase (shown in Figure 7a) and second, a turbulent channel flow velocity profile (Cp) for gas phase with a linear velocity profile for liquid phase (ranging from 0 to $2w_{\text{liq}}$) (shown in Figure 7b). The plots of these velocity profiles for each simulation case is shown in Figure 7. The equations

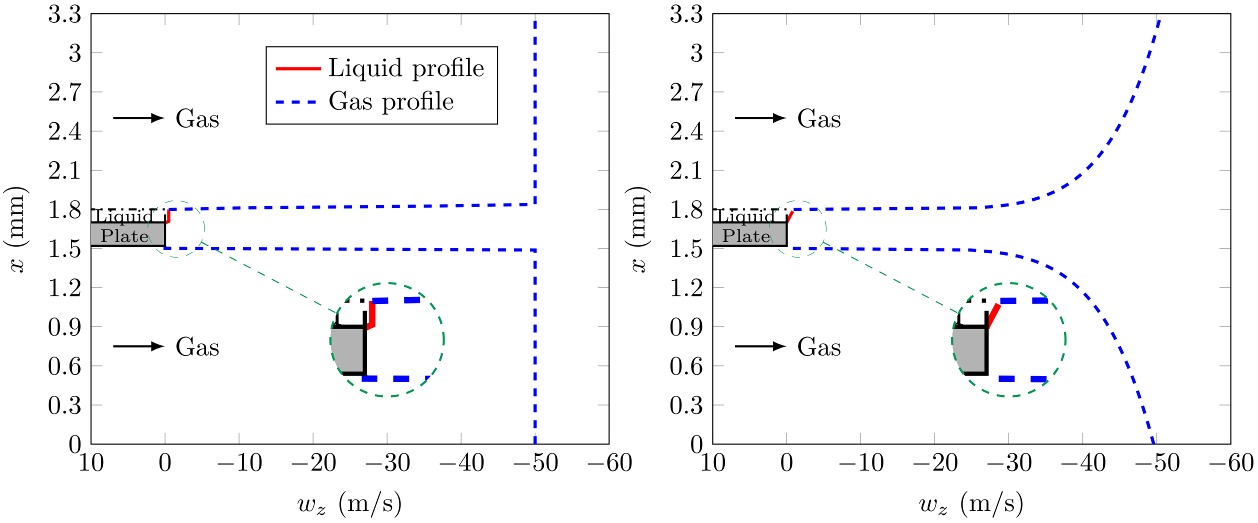

(a) Flat profile (Fp)

(b) Channel flow profile (Cp)

Figure 7: Velocity profile plots for liquid phase (—) and gas phases (- - -). In (a): flat profile (plug flow) for liquid and gas phases; (b) linear velocity profile for liquid and channel flow profile for gas phase.

for the velocity for the flat profile (Fp) case are given as

$$
\begin{aligned}
u &= 0 \\
v &= 0 \\
w(x) &= \begin{cases} -w_{\text{gas}}, & 0 \le x < h_{\text{gas}} \\ 0, & h_{\text{gas}} \le x < h_{\text{gas}} + h_{\text{pf}} \\ -w_{\text{liq}}, & h_{\text{gas}} + h_{\text{pf}} \le x < h_{\text{gas}} + h_{\text{pf}} + h_{\text{liq}} \\ -w_{\text{gas}}, & h_{\text{gas}} + h_{\text{pf}} + h_{\text{liq}} \le x \le 2h_{\text{gas}} + h_{\text{pf}} + h_{\text{liq}}, \end{cases}
\end{aligned}
\tag{12}
$$

and the equations for the velocity for the channel profile (Cp) case are given as

$$
\begin{aligned}
u &= 0 \\
v &= 0 \\
w(x) &= \begin{cases} w_{\text{gas},1}, & 0 \le x < h_{\text{gas}} \\ 0, & h_{\text{gas}} \le x < h_{\text{gas}} + h_{\text{pf}} \\ -\left(\frac{2w_{\text{liq}}}{h_{\text{liq}}+\Delta x/2}\right)(x - (h_{\text{gas}} + h_{\text{pf}})) & h_{\text{gas}} + h_{\text{pf}}, \le x < h_{\text{gas}} + h_{\text{pf}} + h_{\text{liq}} \\ w_{\text{gas},2}, & h_{\text{gas}} + h_{\text{pf}} + h_{\text{liq}} \le x \le 2h_{\text{gas}} + h_{\text{pf}} + h_{\text{liq}} \end{cases}
\end{aligned}
\tag{13}
$$

where the values of $w_{\text{gas},1} = -w_{\max}\left(1 - \frac{|x-(h_{\text{liq}}-h_{\text{chw}})|}{h_{\text{chw}}}\right)^{1/7}$ and $w_{\text{gas},2} = -2w_{\text{liq}} - w_{\max}\left(1 - \frac{|x-(h_{\text{gas}}+h_{\text{pf}}+h_{\text{liq}}+h_{\text{chw}})|}{h_{\text{chw}}}\right)^{1/7}$ with $w_{\max} = (8/7)w_{\text{gas}}$. The value of $w_{\max}$ is obtained by matching the total mass flow rate to that of the atomizer channel†. For each simulation case, the computational domain (Figure 3a) is discretized using a mesh of about 33.5 million cells resulting in an equidistant mesh spacing $\Delta x = 12.89\,\mu\text{m}$. The simulation is run on 1024 cores upto 14 ms of physical time with the data written to disk approximately every 35 µs consuming a total of 221,184 CPU hours for Fp case and 122,880 CPU hours for Cp case.

4. Results and discussion

We now present the results from the simulation of the primary atomization of the airblasted liquid sheet. First, qualitative analyses of the breakup physics and atomization mechanisms will be presented. A comparison of these mechanisms will be made between the two inlet velocity profile simulation cases. Then, quantitative data extracted from the simulations, such as drop size distribution (DSD) and drop velocity distribution (DVD), are presented. These quantities are vital for the subsequent Lagrangian particle simulations for the secondary atomization of drops. To investigate the presence of secondary atomization of the drops occurring in the simulations, the DSD and number based frequency distribution of drop diameters along with the drop-based Weber number at different downstream sampling locations are compared. Following the secondary atomization studies, the extraction of near-field quantities such as lengths and velocities of liquid ligaments formed in the accumulated liquid region at the edge of the pre-filmer plate are presented. It is to be remarked that this work is one among the initial simulation studies [22] in which such a novel methodology of extraction such near-field data is employed.

4.1. Breakup mechanisms

The airblast atomization process is comprised of many breakup mechanisms of which two predominant mechanisms found in the literature [43, 9] are sheet/bag breakup and ligament breakup. These atomization

---

[†] The derivation is according to $\int_0^{h_{\text{channel}}} w(x)dx = h_{\text{channel}} \times w_{\text{gas}} \Rightarrow \int_0^{h_{\text{channel}}} \underbrace{w_{\max}\left(1 - x/h_{\text{channel}}\right)^{\frac{1}{7}}}_{\text{Turbulent channel profile}} dx = h_{\text{channel}} \times w_{\text{gas}} \Rightarrow w_{\max} = (8/7)w_{\text{gas}}$ where $h_{\text{channel}} = 8.1\,\text{mm}$.

mechanisms are also observed in our simulations for both the inlet velocity profile cases. Figures 8 and 9 show several instantaneous snapshots of the liquid/gas interface shown in blue color (obtained as the zero isolevel of the level set function) for the flat profile (Fp) and channel profile (Cp) simulation cases, respectively. The flow of the liquid and gas is from the top to bottom in these figures. The breakup process in the planar pre-filming airblast atomization is as follows: due to difference in the momentum flux between liquid and gas phases, instability waves are generated in the liquid sheet on top of the pre-filmer plate (c.f. Figures 8b and 9b) causing liquid shear thereby collecting the liquid parcel towards the trailing edge of the pre-filmer plate forming a liquid reservoir (see Figure 1). From this reservoir, thin sheets and long ligaments of liquid are formed (c.f. Figures 8b, 9b and 9d) which then develop holes (c.f. Figures 8c, 8d and 9c) since the surface tension cannot counteract the disintegration process. The holes penetrate the sheet causing breakup into various sized droplets (c.f. Figures 8d and 9c) and long ligaments break up into bulgy and medium-sized droplets (c.f. Figures 8e, 9e and 9f). We can observe that the number of drops generated for the Cp case is less than that of the Fp case. This is due to the fact that the Fp velocity is a violently turbulent profile with a sharp gradient between the liquid and gas profile than that of Cp velocity (c.f. Figure 7) thereby causing the burst of drops.

These observations are consistent with the torn sheet/bag breakup regime described by Fernández et al. [76] for the operating point employed in this work. It is speculated that the instability waves on the liquid film are formed due to the Kelvin-Helmholtz (KH) instability, however, this conjecture is still to be verified. Moreover, a global qualitative similarity in the destabilization of the interface is observed between the simulation cases. It is to be remarked that there was no dewetting of the plate observed in the simulations. Moreover, the flapping of the liquid sheet (observed in side view $x-z$ plane) was found to be asynchronous to the atomization, i.e., the frequency at which droplets and ligaments detatch from the liquid sheet is different from the frequency of the flapping of the sheet. The quantification of these frequencies is beyond the scope of this work.

To get a global picture of the sheet flapping, atomization, and the turbulent velocity imposed, Figure 10 shows two instantaneous snapshots from Fp and Cp cases along with the contours of the velocity magnitude. From this figure, it is indeed obvious that the velocity field is highly turbulent causing the destabilization of the liquid sheet and its subsequent atomization. Moreover, we can observe the disintegration of large drops and formation of thin sheet as well as long ligaments at the trailing edge of pre-filmer plate.

4.1.1. Sheet/bag breakup

One of the dominant droplet breakup mechanisms observed in the airblast atomization simulations is the sheet/bag breakup. Figure 11 shows a series of instantaneous snapshots of the visualization of the liquid sheet breakup into drops for the Fp case. In this breakup mechanism, the accumulated liquid at the trailing edge of the pre-filmer plate forms a bag like structure (c.f. Figure 11a) which is then pushed up due to the aerodynamic forces from the high speed air flowing below the pre-filmer plate. This bag then develops holes (c.f. Figure 11b) partly due to the surface tension failing to counteract the disintegration phenomenon (i.e., physical effect) and partly due to the mesh resolution employed in the simulations (i.e., numerical effect). This hole quickly penetrates through the surface of the sheet (c.f. Figure 11c) thereby forming droplets (c.f. Figure 11d) whose diameters are of the size of the thickness of the sheet. Such a sheet/bag breakup mechanism is commonly found in the flows with high shear. It is to be remarked that the same physical mechanism of sheet breakup is observed in the Cp case.

4.1.2. Ligament breakup

The next predominant breakup mechanism observed in the simulations is the ligament breakup mechanism. Figure 12 shows a series of instantaneous snapshots of the flow visualization extracted from the Fp simulation case. The liquid accumulated as reservoir at the trailing edge of the pre-filmer plate (see Figure 1 for the location of trailing edge) forms ligaments. These ligaments, shown in Figure 12a, are subjected to high aerodynamic forces from the air flowing above and below the pre-filmer plate. These forces stretch the ligament (c.f. Figure 12b) upto a point when its diameter is smaller than the employed computational mesh spacing. It is at this point the breakup of the ligaments into droplets (of the size of diameter of ligaments)

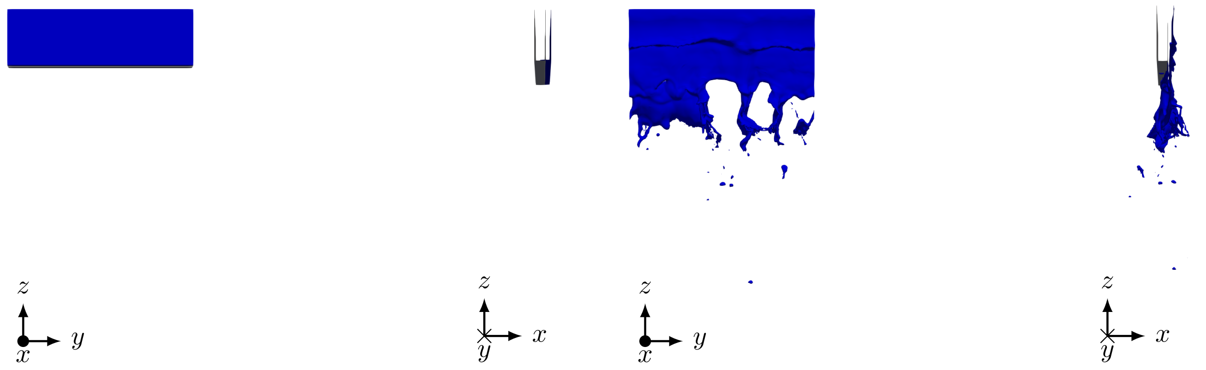

(a) $t = 0.00\,\mathrm{ms}$

(b) $t = 1.36\,\mathrm{ms}$

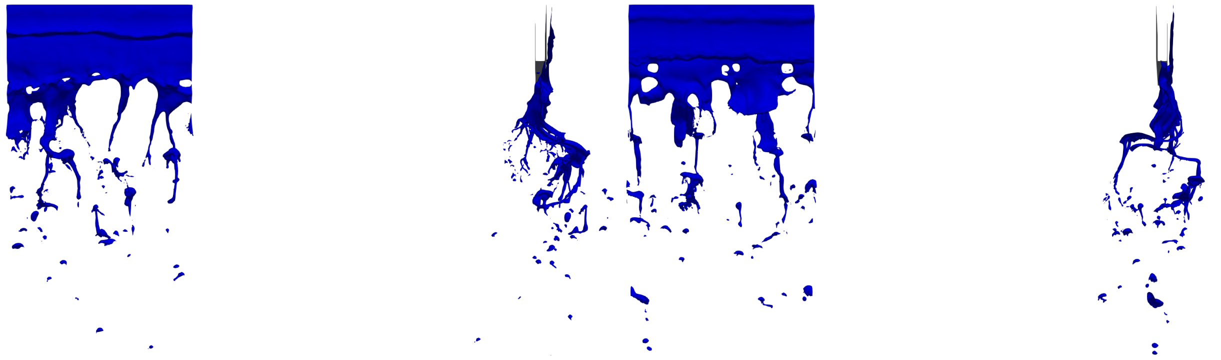

(c) $t = 1.69\,\mathrm{ms}$

(d) $t = 5.79\,\mathrm{ms}$

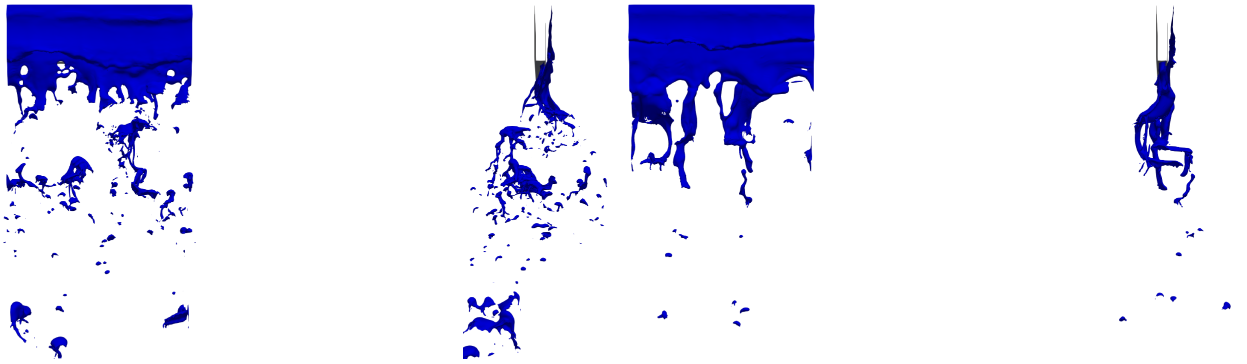

(e) $t = 8.13\,\mathrm{ms}$

(f) $t = 10.32\,\mathrm{ms}$

Figure 8: Instantaneous snapshots of liquid sheet destabilization and atomization into ligaments and droplets for the flat profile (Fp) simulation case.

occur due to Rayleigh-Plateau instability (c.f. Figures 12c and 12d). The identical breakup mechanism is observed in the Cp case as well.

For the purposes of illustration, Figure 13 show instantaneous snapshots of the different breakup mechanisms along with the cluster of produced droplets rendered using Blender visualization software.

4.2. Droplet analysis

Having presented the qualitative results so far, we now present the quantitative results pertaining to the atomized drops in this subsection. Among the many quantitative results extracted from the simulations, the drop size distribution (DSD) and drop velocity distribution (DVD) are pivotal in designing the combustion chamber of the aero engines. The size and velocity of the drop have direct influence on its rate of fuel

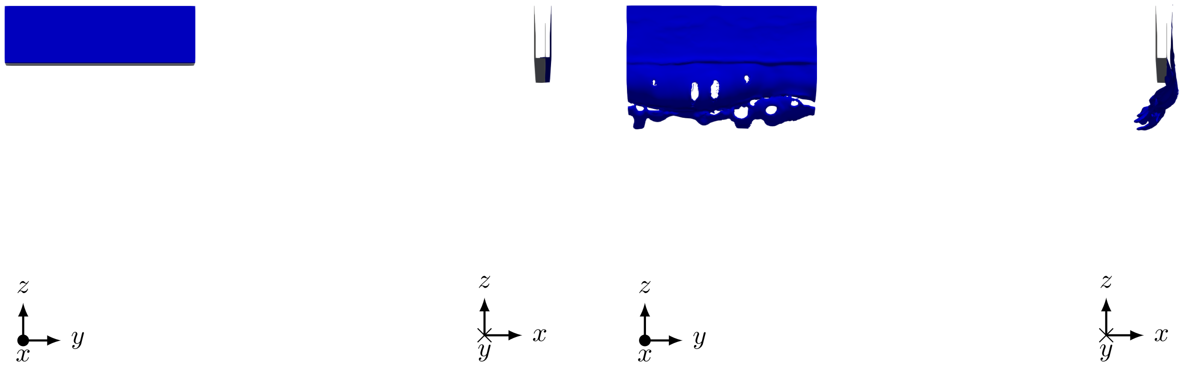

(a) $t = 0.00\,\mathrm{ms}$ (b) $t = 1.40\,\mathrm{ms}$

(c) $t = 1.68\,\mathrm{ms}$ (d) $t = 5.81\,\mathrm{ms}$

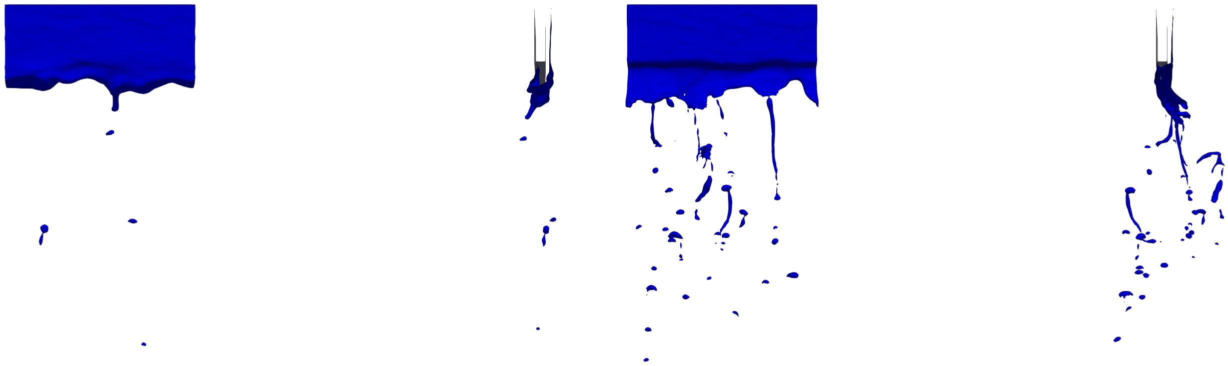

(e) $t = 8.12\,\mathrm{ms}$ (f) $t = 10.34\,\mathrm{ms}$

Figure 9: Instantaneous snapshots of liquid sheet destabilization and atomization into ligaments and droplets for the channel profile (Cp) simulation case.

evaporation and its subsequent combustion. In fact, the DSD and DVD are also useful for secondary atomization simulations using Lagrangian and Eulerian approaches as well as primary atomization modeling for which the droplets of certain size are injected along a specific trajectory with a certain velocity [77]. Therefore, it is imperative to understand and analyze the DSD and DVD for the retro-improvement of the injector design. In order to obtain these distributions, the extraction of atomized droplet (or a liquid structure) from the simulations is necessary. To that end, such liquid structures are identified using a connected component labelling (CCL) structure detection algorithm [78] for each sampled time step from the simulations. Each sampling from the simulations is written to disk approximately every 35 µs of physical time containing the three dimensional data of the computational domain including velocity, level set, liquid volume fraction data along with the statistical information about the liquid structures. The information

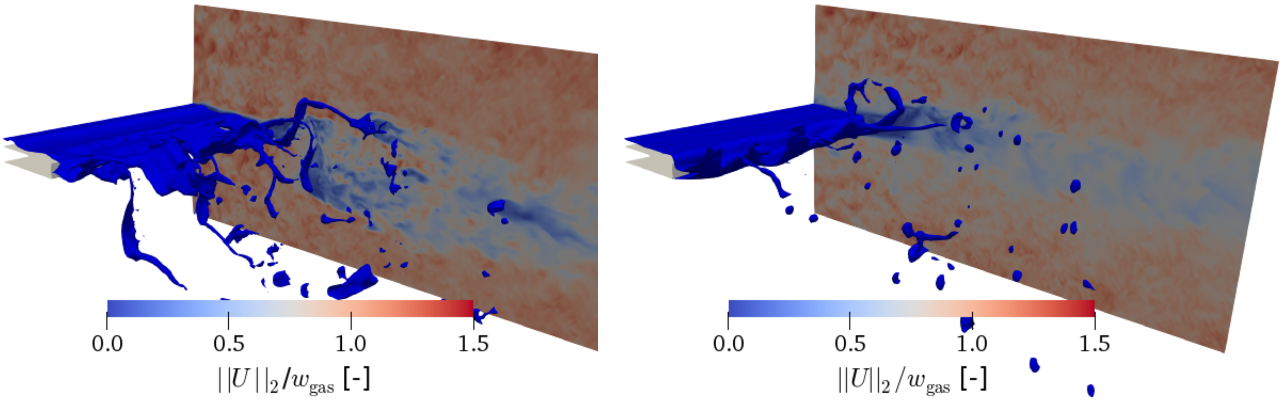

(a) Flat profile (Fp)

(b) Channel profile (Cp)

Figure 10: Instantaneous snapshots of the atomizing liquid sheet along with the contour of the velocity magnitude for flat profile (Fp) and channel profile (Cp) case.

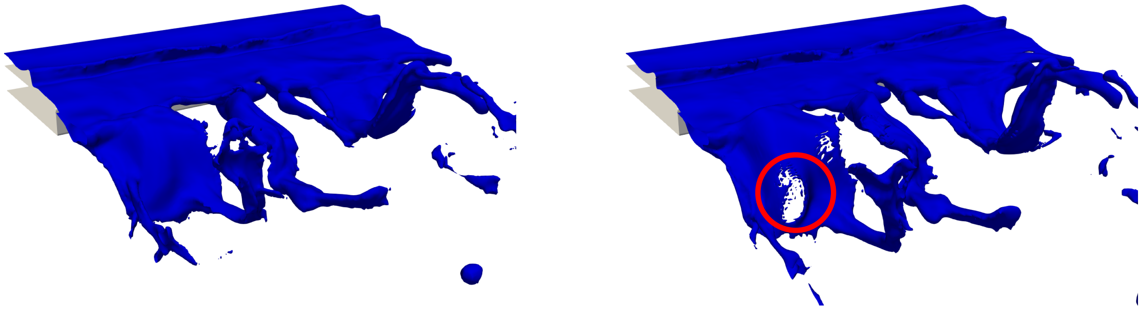

(a) $t = 10.29\,\mathrm{ms}$

(b) $t = 10.32\,\mathrm{ms}$

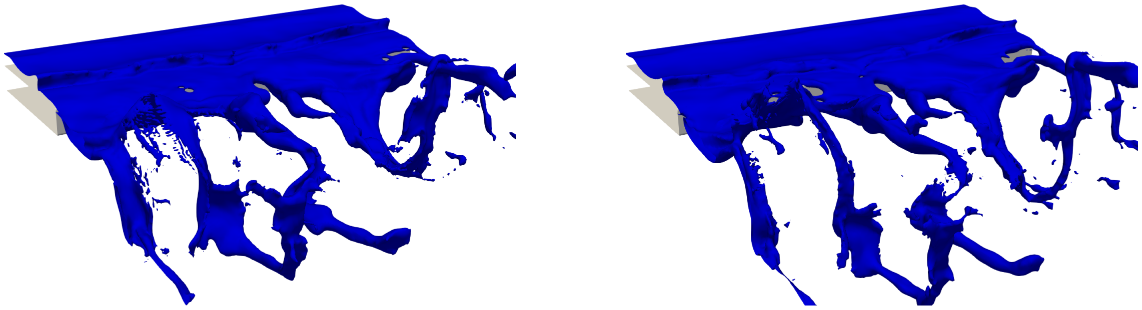

(c) $t = 10.36\,\mathrm{ms}$

(d) $t = 10.39\,\mathrm{ms}$

Figure 11: Sequence of events of sheet/bag breakup mechanism in airblast atomization visualized from simulations using Fp case. (a): formation of liquid bag and sheet-like structure; (b): hole formation and liquid sheet rupture; (c) and (d): sheet breakup into droplets.

collected for each liquid structure include their total volume, total surface area (computed as the sum of the area of PLIC interface spanning over all computational cells belonging to this structure), velocity (volume-weighted velocity from each cell weighted by total volume), and coordinates of the centroid of the structure. The total volume of each of these liquid structures (i.e., drops) is then computed using which an equivalent spherical diameter of each droplet is computed.

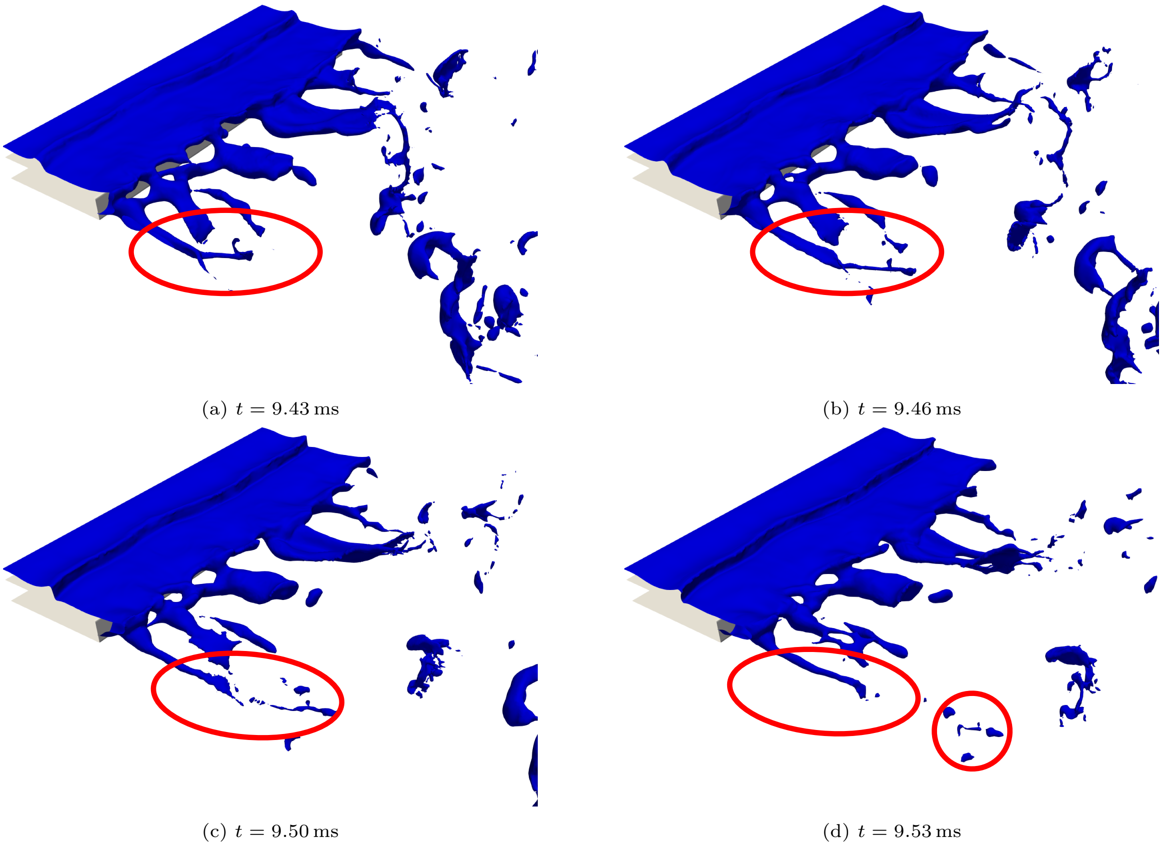
(a) $t = 9.43\,\mathrm{ms}$

(b) $t = 9.46\,\mathrm{ms}$

(c) $t = 9.50\,\mathrm{ms}$

(d) $t = 9.53\,\mathrm{ms}$

Figure 12: Sequence of events for ligament breakup of airblast atomization visualized from simulations for flat profile (Fp) inlet velocity case. (a): formation of ligament from accumulated liquid; (b): stretching and twisting of ligament due to high speed of air; (c): ligament breakup due to Rayleigh-Plateau instability; (d): atomized droplets advected by high speed air.

4.2.1. Drop size distribution

The number-based drop size distribution (DSD) gives the information about the range of the droplet diameters and their probability of presence realized from injection. To construct this distribution from the simulation data, the drops detected using the CCL algorithm are collected at the downstream exit plane of the computational domain, i.e., at $z = -6.6\,\mathrm{mm}$. The diameters of the collected drop (d_{drop}) are binned to obtain a probability density function (PDF) of the DSD.

Figure 14 shows the plot of the PDF of DSD for the Fp and Cp simulation cases along with the experimental data [22]. It can be seen that the profile of the experimental data has multiple peaks potentially indicating the presence of multiple atomization mechanisms. We observed sheet breakup (c.f. Section 4.1.1) and ligament breakup (c.f. Section 4.1.2) mechanisms of atomization for this configuration, hence, it would be sensible to associate them to the PDF of DSD plots. It is noteworthy to mention that the drops and web of ligaments produced from the sheet breakup would be of the same size of the sheet thickness. The thickness of these sheets are many orders of magnitude smaller than the mesh spacing Δx. Hence, it becomes very challenging to capture the sheet breakup mechanism using the mesh resolutions employed in this work. However, the drops produced from the ligament breakup mechanism are larger in size than the mesh spacing, hence, it is feasible to capture them in the simulations. Therefore, within the context of this work, the dominant peaks in Figure 14 could be attributed to the remnants of the ligament breakup mechanism. It is to be remarked that the smallest diameter measured in the experiments is $20\,\mu\mathrm{m}$, hence, the cut-off of the PDF of the DSD in the experimental profile. A previous work on the airblasted liquid sheet [22] removed (i.e., clipped) the drops whose sizes are smaller than $20\,\mu\mathrm{m}$ when constructing the PDF of DSD for the sake

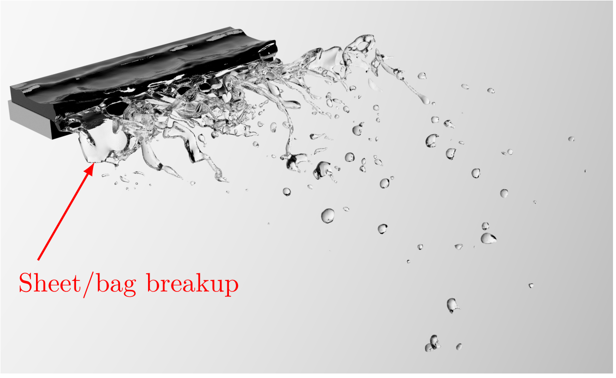

(a) Rendering of the sheet breakup from the simulations.

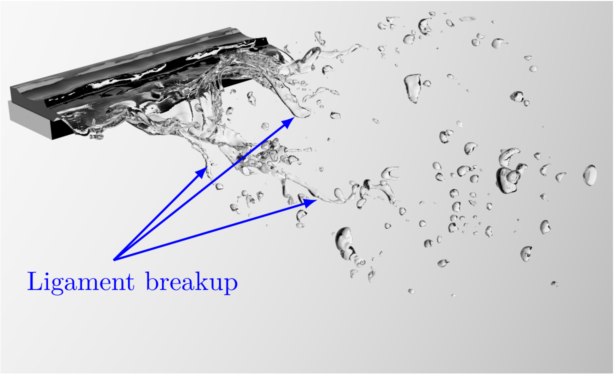

(b) Rendering of the ligament breakup from the simulations.

(c) Rendering of varying sized droplets produced.

Figure 13: Predominant breakup mechanisms observed in airblast atomization simulations for the flat profile (Fp) c_1^{Fp} case.

of comparison with the experimental data. However, such a procedure will alter the profile of the PDF of the DSD giving a skewed measure of the DSD. Hence, to represent the complete PDF in this work, no such clipping or removal of the drops is performed.

The first inference from Figure 14 is that the simulation results are under-predicting the experimental DSD which could be attributed to the employed mesh resolution in the simulations. In fact, a similar under-prediction was also found in the study by Warncke et al. [22] using a diffused interface VOF method of liquid/gas interface reconstruction. Having a finer mesh resolution will indeed prevent the occurrence of premature breakup of drops and ligaments from the liquid sheet thereby improving the statistics of atomization however incurring high computational cost. The next observation is the presence of multiple

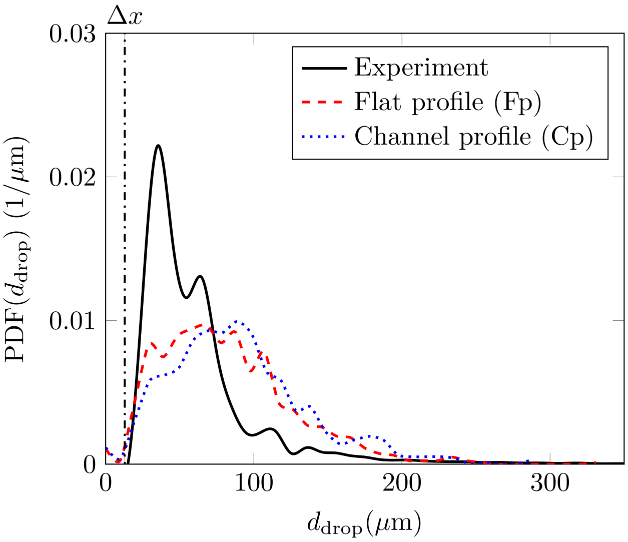

Figure 14: Plot of drop size distribution (DSD) for flat profile (Fp) (- - -) and channel profile (Cp) (⋯⋯) inlet profile cases from the simulations along with experimental data (——) [22]. The dashdotted line (-·-·-) represents the location of the mesh spacing $\Delta x = 12.89\,\mu\text{m}$ in comparison to the drop diameter d_{drop}.

peaks in the PDF of DSD from the simulations for both the Fp and Cp inlet velocity profile cases. Although the DSD profiles of the simulation cases overlap approximately (especially for the small diameter values), there seems to be a non-negligible effect on the atomization characteristics by the change in the inlet velocity profile. For example, the Cp case is yielding relatively higher probability of occurrence of large sized drops than in the Fp case.

Another important atomization characteristic that define the quality of injection along with the DSD is the Sauter Mean Diameter (SMD). This quantity is computed from the experimental and simulation data using the expression

$$\text{SMD} = \frac{\int \text{PDF}(D) D^3 dD}{\int \text{PDF}(D) D^2 dD}; \quad D = d_{\text{drop}}. \tag{14}$$

The SMD computed from the experiments is 154.80 µm while for the Fp case is 130.13 µm and the Cp case is 150.37 µm. First, it can be observed that the SMD values from the simulations are of the same order of magnitude as that of the experiments. Second, the SMD of the Cp simulation case is having an excellent agreement with the experiments indicating its physical relevance as the inlet velocity profile. However, an obvious question is that, if the profiles of the Fp and Cp simulation cases are qualitatively overlapping, how can their SMD values differ? The answer lies in the fact that the SMD is highly sensitive to the presence of drops with large diameter values. As can be seen in Figure 14, the Cp case is yielding relatively higher probability for the large drops than that of the Fp case albeit their qualitative profile matching for the smaller diameters. Overall, the PDF values are in the same order of magnitude as that of the experiments while an under-prediction is observed quantitatively.

4.2.2. Drop velocity distribution

The drop velocity distribution (DVD) is an another important quantity along with the DSD that is useful for the subsequent Lagrangian and Eulerian simulations for primary and secondary atomization modeling. The PDF of the DVD is constructed in the same manner as that of the DSD from the simulations. As part of the connected component labelling (CCL) structure detection algorithm [78], we extract the volume-weighted averaged velocity of the centroid of each liquid structure weighted by the total liquid volume of the structure. After the sampling of the drops at the $z = 6.6$ mm plane, the streamwise component (i.e., w_z component) of the drop velocity is binned to form the PDF of the DVD.

Figure 15 shows the PDF of the DVD for the streamwise component of the droplet velocity with the drops sampled at the exit of the downstream direction. It is to be remarked that the drop velocities are negative values consistent with the negative $z-$axis oriented towards downstream direction (c.f. Figure 3a). Analyzing this plot, we can first observe that that the results from the simulation for both the flat profile and channel profile cases are agreeing very well with the experimental data. Second, the Fp simulation case quantitatively over-predicts the probability peak and under-predicts the location of the peak in drop velocity. Moreover, we can also see that the Cp simulation case under-predicts the probability of the larger as well as smaller drop velocities however, the profile of its curve towards the larger magnitude of the negative velocities follows the same trend as the experiments. Third, the location of the peak value of the DVD (i.e., the value of drop velocity for which the peak of the DVD is attained) for the Fp case is 12.36 m/s, the Cp case is 11.10 m/s while that from the experiments is 13.2 m/s which are evidently in the same order of magnitude agreement. Finally, there is an observed effect of the change of inlet velocity profile from flat profile to channel profile resulting in a wider distribution of velocity and the peak of the PDF curve occur at a lower value of drop velocity $w_{z_{\text{drop}}}$. This is because the shear near the liquid film is larger with a flat velocity profile and as a consequence the slip velocity between liquid and gas phase becomes large resulting in larger drop velocities. In summary, inlet velocity profile does have an effect on the DVD of the liquid in the simulations and an overall good agreement between the simulations and the experiments is observed.

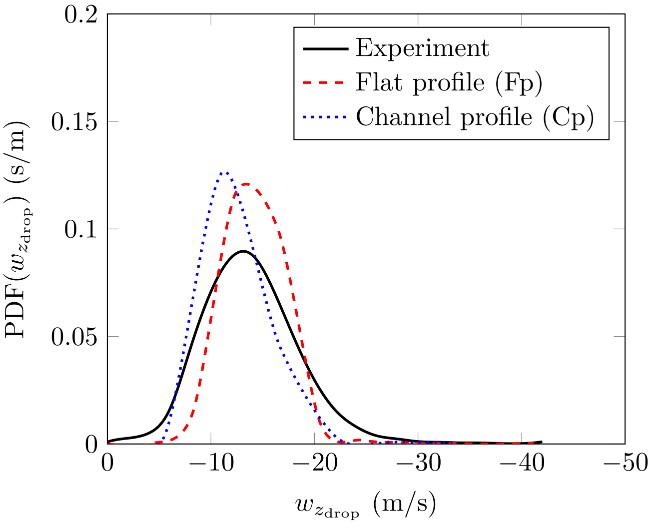

Figure 15: Plot of drop velocity distribution (DSD) for flat profile (Fp) (- - -) and channel profile (Cp) (······) inlet profile cases from the simulations along with experimental data [22] (——).

4.2.3. Secondary atomization

Many of the previous studies on experimental [19, 20, 9, 21] and numerical [22, 23, 24, 25] investigations of airblast atomization of liquid sheet have focused entirely on the primary atomization. However, it is physically and statistically possible that the atomized drops produced from various breakup mechanisms can undergo secondary atomization within the computational domain. The data about the presence of secondary atomization for airblast atomization will be directly helpful for the secondary breakup modeling (SBM) that focuses on developing breakup models based on aerodynamic forces and turbulence.

In order to investigate the existence of the secondary atomization of the drops in this work, we have computed the PDF of the DSD at various downstream locations (i.e., along the $z-$direction) as shown in Figure 16 for both the flat profile and channel profile simulation cases. From these plots, we can see that PDF curves do not collapse into a single curve for both these cases for any of the sampling location. The collapse of these curves will clearly indicate that there are no more drop breakup/drop coalescence events occurring in the domain. However, the inference otherwise is observed from both the cases of simulation results. Moreover, the peaks of the PDF curves keep shifting towards the higher drop diameter d_{drop} values. This could be attributed to the occurrence of drop coalescence, i.e., smaller drops aggregate to form bigger drop (c.f. Figure 19). Furthermore, when comparing the Fp (Figure 16a) case and Cp case (Figure 16b), we can find that: first, the probability of finding small sized drops is higher for Fp case than that of Cp case; second, the degree of decrease in the probability of drop sizes moving along the downstream sampling locations is lesser for the Cp case than that of Fp case. From these inferences, it can be concluded that there is lower probability of occurrence of secondary atomization however, higher probability of drop coalescence.

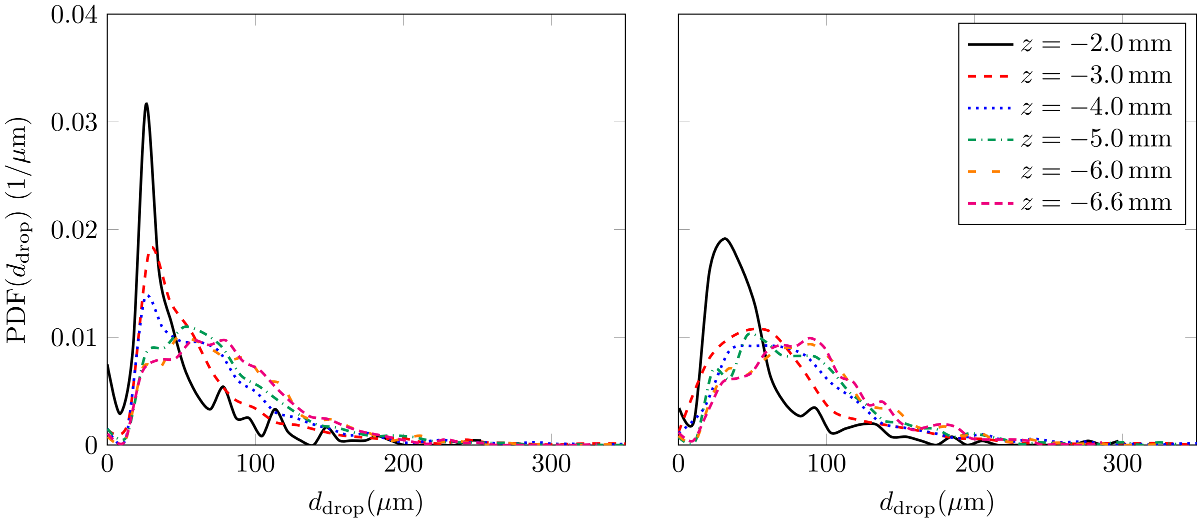

(a) Flat profile (Fp) case

(b) Channel profile (Cp) case

Figure 16: PDF of DSD sampled at various downstream locations of $z = -2$ mm (——), -3 mm (- - -), -4 mm (·····), -5 mm (-·-·-), -6 mm (- -), -6.6 mm (----) from flat profile (Fp) and channel profile (Cp) simulation cases.

To further investigate, we show in Figure 17 the plots of the evolution of the number based frequency distribution of sampled drop diameters. In this plot, N_{sum} is the sum of the frequency values of drop diameters over all sampling locations and over all sampled time steps. This plot, unlike the PDF plot (c.f. Figure 16), is devoid of the constraint to keep the area under the curve equal to unity which changes the location of the peak of the PDF. Hence, from these plots, it is possible to make a convincing argument towards the evolution of the drop diameters in the downstream direction. It can be seen that frequency distribution curves measured at various downstream locations do not collapse. In addition, we can see (for both the Fp and Cp cases) that the number of drops found at various sampling locations decreases when moving along the downstream direction, suggesting the occurrence of drop coalescence. Moreover, it can be inferred that peak of these *number based* frequency distribution curves indeed move towards the higher drop diameter values when the sampling location changes indicating formation of large drops. That being said, there is a non-negligible probability of occurrence of secondary atomization in the simulations since decrease of the number of small sized drops is not by an order of magnitude smaller between the sampling locations. When comparing the Fp case (Figure 17a) and Cp case (Figure 17b), we can observe that the number of drops produced for the Cp case near the pre-filmer plate edge sampling location is higher than Fp case. This is because the number of sampled drops from the Cp case is lower than that for the Fp case due to their respective atomization modes influenced by the inlet velocity profiles (c.f. Figures 8 and 9).

To make a conclusive argument about the presence of secondary atomization and drop coalescence, we now show in Figure 18 the plots of the evolution of the Sauter Mean Diameter (SMD) computed at the different downstream sampling locations from the diameters of the sampled drops. The SMD values at various downstream sampling locations are computed using the Equation (14). There is an observed increase in the SMD values along the downstream between $z = 1.5$ mm to $z = 3$ mm after which there is an observed

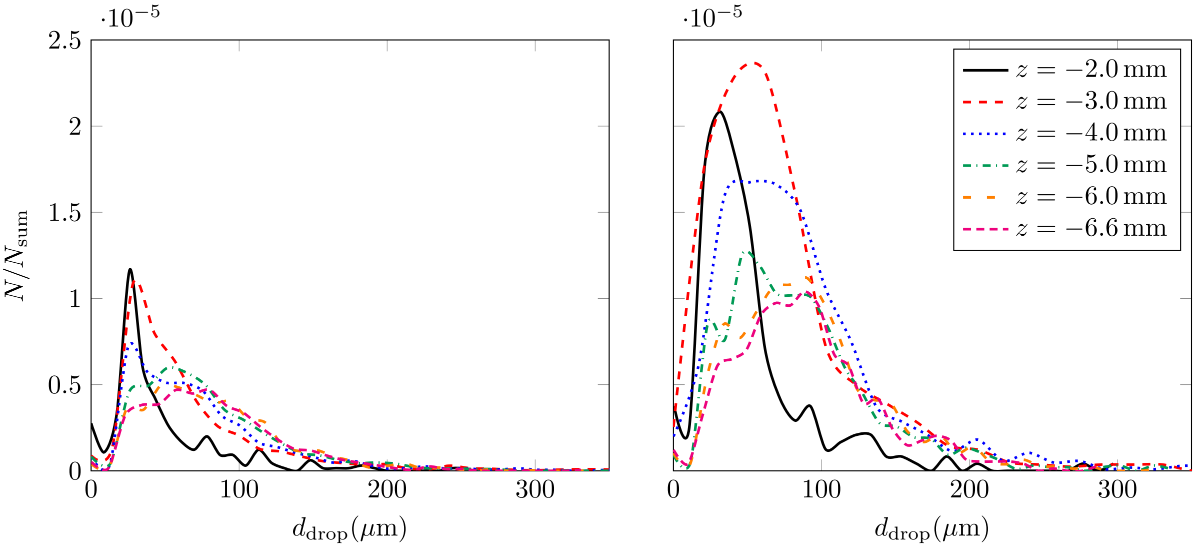

(a) Flat profile (Fp) case

(b) Channel profile (Cp) case

Figure 17: Number based frequency distribution of drop diameters sampled at various downstream locations of $z = -2\,\mathrm{mm}$ (——), $-3\,\mathrm{mm}$ (- - -), $-4\,\mathrm{mm}$ (⋯⋯), $-5\,\mathrm{mm}$ (-·-·-), $-6\,\mathrm{mm}$ (- -), $-6.6\,\mathrm{mm}$ (- - -) from flat profile (Fp) and channel profile (Cp) simulation cases.

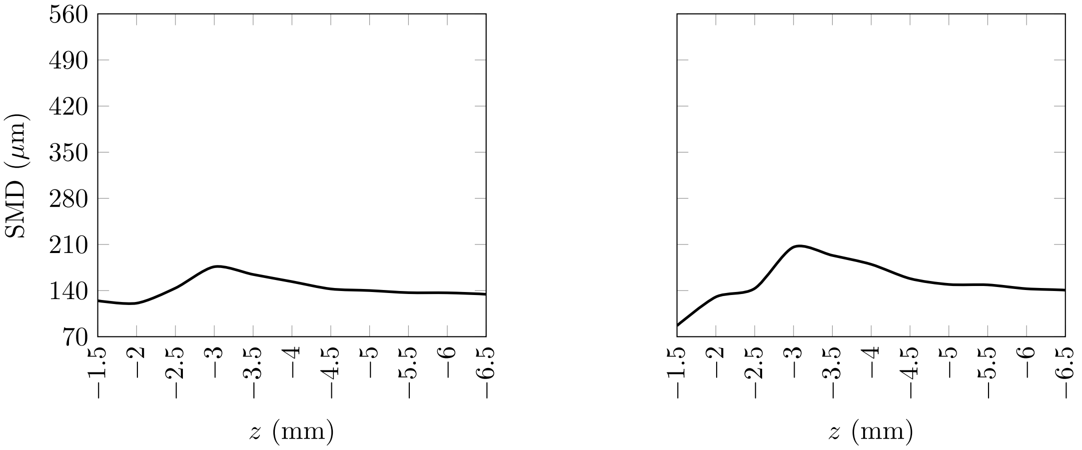

(a) Flat profile (Fp) case

(b) Channel profile (Cp) case

Figure 18: Evolution of Sauter Mean Diameter (SMD) of drops along downstream direction for flat profile (Fp) and channel profile (Cp) simulation cases.

decrease. The increase in the SMD could be attributed to the aggregation of the drops stripped from the liquid film and ligament breakup mechanism. An exemplary case of such a drop merging event occurring in the Fp simulation case is shown in Figure 19 and similar events are observed to occur for the Cp case as well. Since the SMD value is sensitive to the presence of large drops, these intermittent drop merging events are directly influencing the increase of SMD. However, the decrease in its value downstream could be attributed to the breakup of these large drops due to aerodynamic forces. It can be observed that the choice of the inlet velocity profile for the liquid and gas does seem to have an effect on the peak SMD value. Hence, from these inferences, it can be concluded that there is equal probability of secondary atomization and drop coalescence in the computational domain. At this juncture, it is noteworthy to point out that

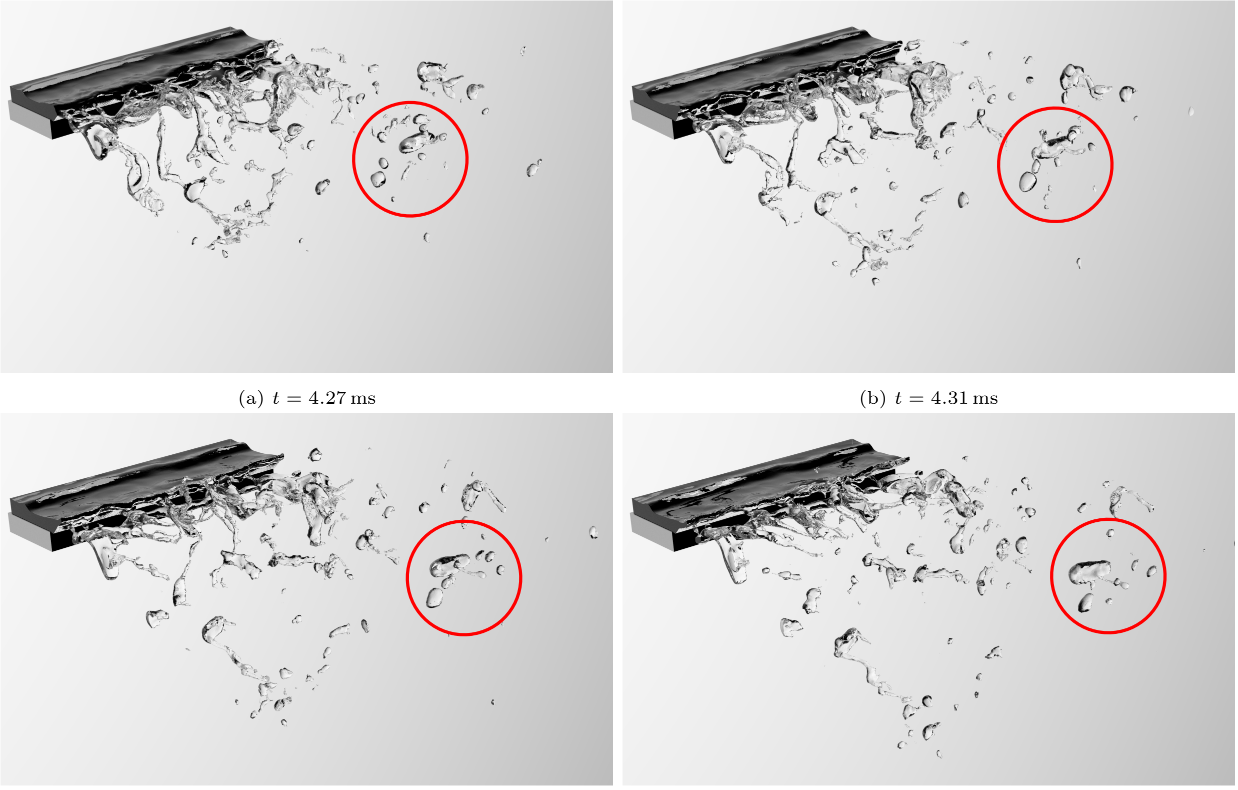

(a) $t = 4.27\,\mathrm{ms}$ (b) $t = 4.31\,\mathrm{ms}$

(c) $t = 4.34\,\mathrm{ms}$ (d) $t = 4.37\,\mathrm{ms}$

Figure 19: Drop coalescence observed in flat profile (Fp) case.

Figures 18a and 18b are in excellent agreement with the work of Chaussonnet et al. [50] (see Fig. 21 in this reference) thereby validating our simulation results with the literature.

Finally, to validate the occurrence of the secondary atomization of drops, we have computed an approximate drop-based Weber number according to

$$\mathrm{We}_{\mathrm{drop}} = \frac{\rho_{\mathrm{gas}}(w_{\mathrm{gas}} - w_{z_{\mathrm{drop}}})^2 d_{\mathrm{drop}}}{\sigma}. \tag{15}$$

Scatter plots of the drop velocity and drop diameter colored by $\mathrm{We}_{\mathrm{drop}}$ for all the sampled drops collected (counted once) from various sampling locations are shown in Figure 20. On observing the scatter plot, it can be seen that there are large number of drops with a velocity around $8\,\mathrm{m/s}$ for all the investigated cases. Moreover, a number of small sized drops (located in the downstream of the domain) with a high velocity are found. These drops attain very high velocity mainly due to their low Stokes number thereby carried away with the gas phase flowing at a speed of $50\,\mathrm{m/s}$. We can find that large droplets with velocities between $0\,\mathrm{m/s}$ and $10\,\mathrm{m/s}$ which are part of the liquid film injected on the pre-filmer plate. These drops have no significant contribution to DSD and DVD computation. Furthermore, the inlet velocity profile does not seem to have an effect on the distribution of the drop diameter and velocity. According to Pilch and Erdman [79], drops with Weber number $\mathrm{We} < 12$ will experience no secondary atomization due to aerodynamic forces while the drops with Weber number in the range $12 \leq \mathrm{We} \leq 50$ experience further atomization due to bag breakup mechanism. We found that about 38% and 42% of the total number of drops are having $\mathrm{We} \leq 12$ for the Fp and Cp cases, respectively. Since majority of the drops (i.e., 62% in Fp case and 58% in Cp case) are having $\mathrm{We} > 12$, it can be concluded that there will be higher probability of occurrence of secondary atomization in the computational domain for both the inlet velocity profile cases. In summary, there is evidence of occurrence of both secondary atomization as well drop coalescence in both the simulation cases.

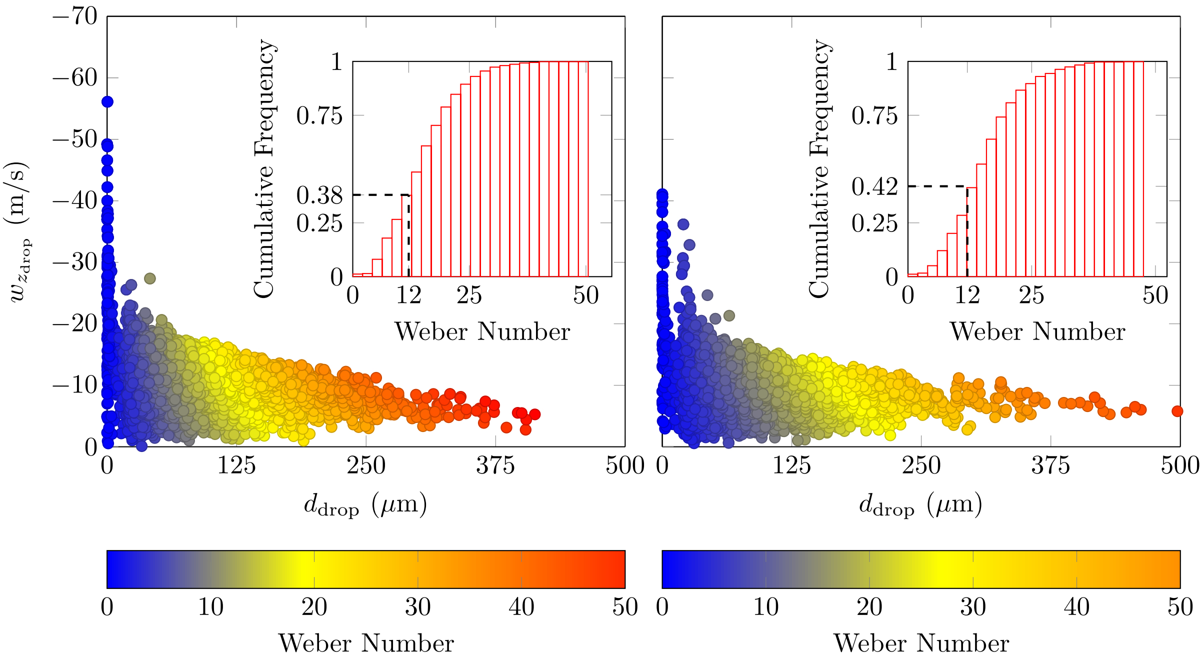

(a) Flat profile (Fp) case

(b) Channel profile (Cp) case

Figure 20: Scatter plot of drop diameter d_{drop} and streamwise component of drop velocity $w_{z_{\text{drop}}}$ colored by drop-based Weber number (We) for flat profile (Fp) and channel profile (Cp) simulation cases.

4.3. Ligament analysis

Aside from the sheet breakup mechanism, the ligament breakup mechanism is one of the dominant atomization mechanism found in our data. The liquid ligaments are formed at the trailing edge of the pre-filmer plate (refer Figure 1) predominantly as shown in Figure 12. They are then stretched to their limit due to the aerodynamic forces from the high speed gas flowing above and below the pre-filmer plate and then breakup into droplets. In the past studies, the quantitative data extracted from the simulations [23, 24, 42] and experimental measurements [29, 28, 30] pertain mainly to the far downstream quantities such as DSD and DVD. In a recent study [9], the data in the near-field region of the injector pertaining to liquid ligaments have been extracted. Such near-field primary breakup data are immensely useful for understanding the physics of atomization.

As part of the ligament analysis, we computed the breakup lengths and velocities of the extracted ligaments. Both these quantities are useful in computation of breakup frequency which is loosely connected to the flapping frequency of the liquid sheet useful in studying the dynamics of liquid atomization. The following subsections present the procedure and the methodology of computation of the ligament breakup length and ligament breakup velocity in the near-field region of the pre-filmer plate.

4.3.1. Ligament breakup length

As part of the near-field data extraction, we first compute the breakup length of the ligaments. To that end, it is imperative to first detect and identify the ligaments from the accumulated liquid at the trailing edge of the pre-filmer plate. We first present the procedure [22] to identify the ligaments and compute their lengths. The length of a ligament l_{lig} is defined as the distance between the edge of the pre-filmer plate and the tip of the liquid structure (from the accumulated liquid) extended in the downstream direction as shown in Figure 21.

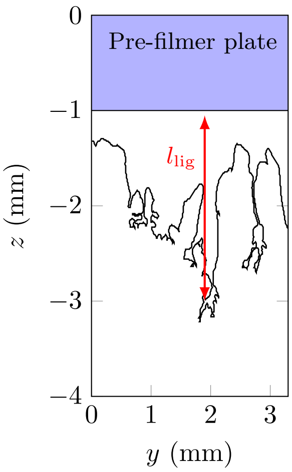

Figure 21: Measurement of ligament length (l_{lig}) from the trailing edge of pre-filmer plate.

The identification and extraction of ligament length from the accumulated liquid in the pre-filmer plate edge is challenging. This is because the interface at the trailing edge experiences high shear and aerodynamic forces making it difficult to distinguish between interface wrinkle and a liquid ligament. To mitigate this issue, we have used a ligament detection algorithm [22] that is split into four steps [80, 81, 82]. First, the 3D simulation data (c.f. Figure 22a) is reduced to a 2D data that is analogous to the shadowgraphy images (from experiments) by assigning label value of 0 (for gas) and 1 (for liquid) to each computational cell with zero and non-zero liquid volume fraction, respectively. Second, these label values are summed up along cross-stream $x-$direction to generate a projected top view ($y - z$ plane view). Any cell in this top view with a summed label value greater than 1 indicates presence of liquid in this view. Third, a connected component labelling (CCL) algorithm [78] is applied for these summed up label values to identify the biggest liquid structure which forms the accumulated liquid at the trailing edge of pre-filmer plate (c.f. Figure 22c). Finally, the 1D interface contour (c.f. Figure 22b) that characterizes the interface of this accumulated liquid is identified using the method described in Ref. [83, 84] (c.f. Figure 22d). This procedure has been applied to every sampled time step (simulation data written to disk approximately every 35 µs of physical time) since the first breakup event has occurred in the simulations.

The length of the ligament is the computed using the 1D interface contour obtained from the reduction algorithm. The maximum dip in this 1D phase interface along the downstream $z-$direction is used for identifying the ligaments. In order to identify these dips in the interface, we have used a technique to traverse through the 1D contour finding the local maxima (dips) and local minima (rises) with the direction of the dip pointing towards the downstream direction. This is shown in Figure 23 in which the blue solid square indicate the location of local maxima and red hollow circles indicate the location of local minima. The distance of the local maximum dips can be considered a starting point in computing the length of the ligaments. The critical step in this computation is to eliminate the effect of the wrinkling in the interface. To that end, we have employed a technique, following Warncke et al. [22], in which the local maximum dips are eliminated from the list of maximum dips if the streamwise distance (measured along $z-$direction) between adjacent local maximum dips and local maximum rise is less than 50 µm. It is to be remarked that the choice of this threshold is arbitrary and the value of 50 µm is chosen following Warncke et al. [22] such that there is a balance between the elimination of interface wrinkle and the detection of physical liquid ligaments. The remaining local maxima after the filtering process become the liquid ligaments and their length is considered as ligament length l_{lig}.

The ligament breakup length $L_{\mathrm{lig}}^{\mathrm{breakup}}$ is then computed as the *mean* of all ligament lengths over all

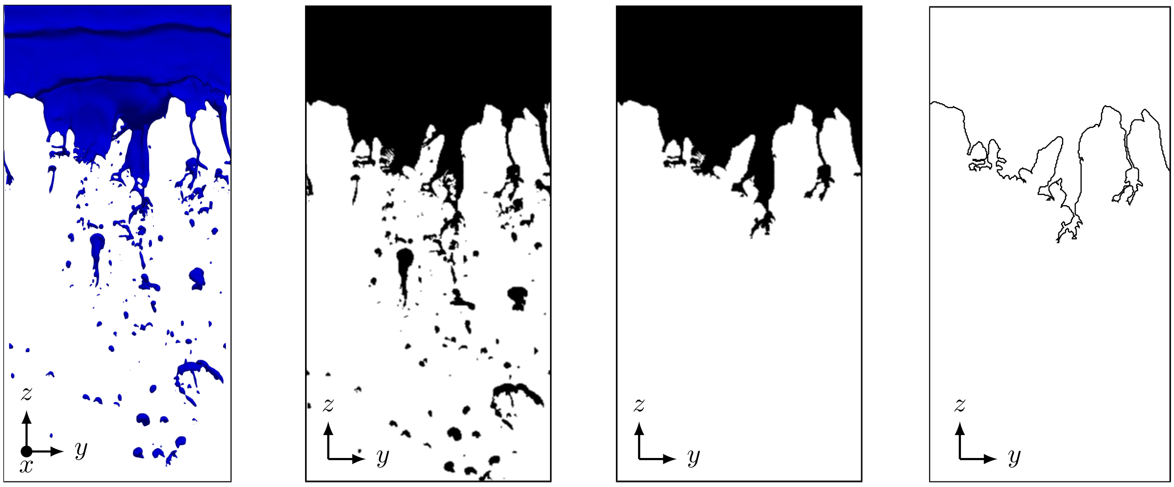

(a) 3D data (b) 2D Projected data (c) Accumulated liquid (d) 1D interface

Figure 22: Reduction of 3D to 1D data for computing ligament characteristics for $t = 5.05\,\text{ms}$ for Fp case.

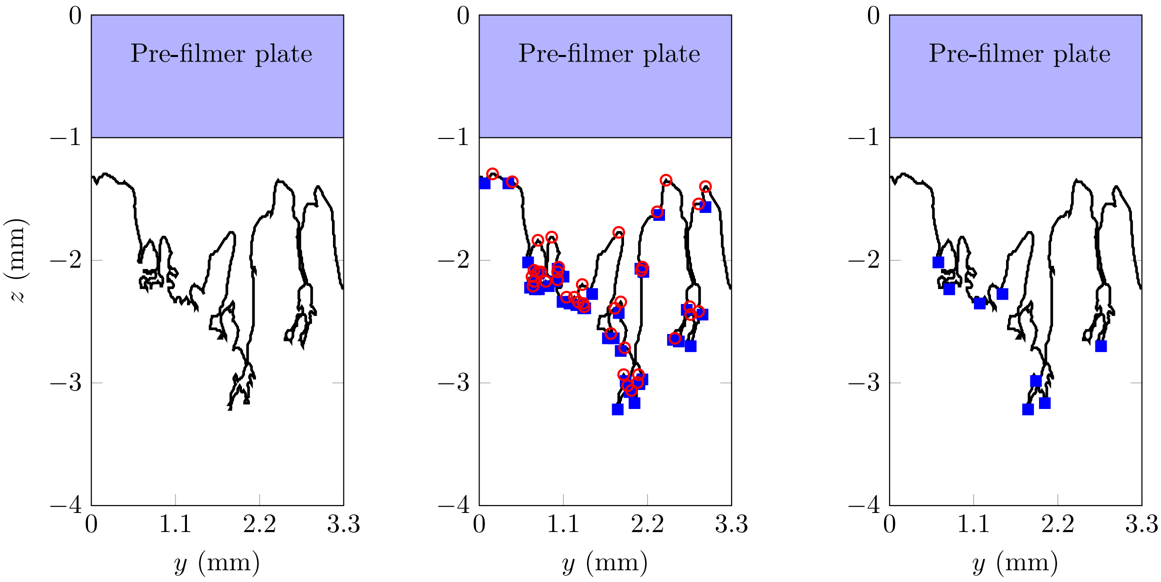

(a) 1D interface contour (b) Local maxima and minima (c) Filtered maxima

Figure 23: Detection and filtering of the local maxima in the 1D interface contour for ligament length computation with local maxima (■) and local minima (○).

sampled time steps from the simulations, i.e.,

$$L_{\text{lig}}^{\text{breakup}} = \frac{\sum_{i=1}^{N} l_{\text{lig}_i}}{N}, \tag{16}$$

where N is the total number of sampled ligaments (i.e., total number of filtered maxima collected over all sampled time steps). Using this expression, the ligament breakup length from the simulations is determined to be $1.32\,\text{mm}$ for the flat profile (Fp) and $1.55\,\text{mm}$ for channel profile (Cp) cases. However, the value of the ligament breakup length measured from the experiments [22] is $3.2\,\text{mm}$. Such an under-prediction has also been observed from the simulations of the literature, for example in Ref. [22] that uses diffused interface capturing method to track the liquid/gas interface. The under-prediction in the simulations could be due to two reasons: first, the fact that we impose a velocity profile at the inlet, unlike Warncke et al. [22] who performed LES of the channel flow; and second, the size of the computational domain along streamwise direction is smaller than the experiments. As mentioned by Warncke et al. [22], the long thin ligaments are found occasionally in the experiments and quite often there existed thin connection between these ligaments and the liquid film in the pre-filmer plate. However, they are detected in the shadowgraphy in the experiments due to a greater time period of recording in comparison to the simulations. To characterize the overall spread of the size of these sampled ligaments, a frequency distribution of the ligament lengths is presented in Figure 24. The maximum measurable length from the simulation is $l_{\text{lig}}^{\text{max}} = L - l_{\text{pf}} = 6.6\,\text{mm} - 1.0\,\text{mm} = 5.6\,\text{mm}$ (since the ligament length is measured from the edge of pre-filmer plate) is also marked in this figure. From this plot, it can be seen that a small number of ligaments of the size larger than the streamwise domain length ($L = 6.6\,\text{mm}$) are detected in the experiments. The simulation results are found to under-predict the length of the liquid ligaments since the peak of the frequency distribution is shifted towards smaller ligament lengths. It is however noteworthy to point out that the ligament length distribution from the Cp case is relatively tending towards the experimental data than the Fp case. This under-prediction could be attributed to under-resolution in the simulations to capture the breakup events. Such an under-resolution often leads to premature breakup of the ligaments from the accumulated liquid structure resulting in smaller value of the sampled ligament lengths. The maximum ligament length measured from the experiments is 8.75 mm while that from the simulations is 3.75 mm for both the Fp and Cp cases. This could be due to multiple reasons: first, there was greater time period for the sampling in the experiments, and therefore, a higher amount of samples compared to the simulations; second, the time spacing between consecutive data write to the hard disk is relatively high; and finally, the field of view of measurement for experiments are larger than that of the simulations, thus, longer ligament lengths that are greater than the length of the streamwise direction of the computational domain are observed. In summary, it can be concluded that the ligament breakup length obtained from the simulations are of the same order of magnitude as that of the experiments.

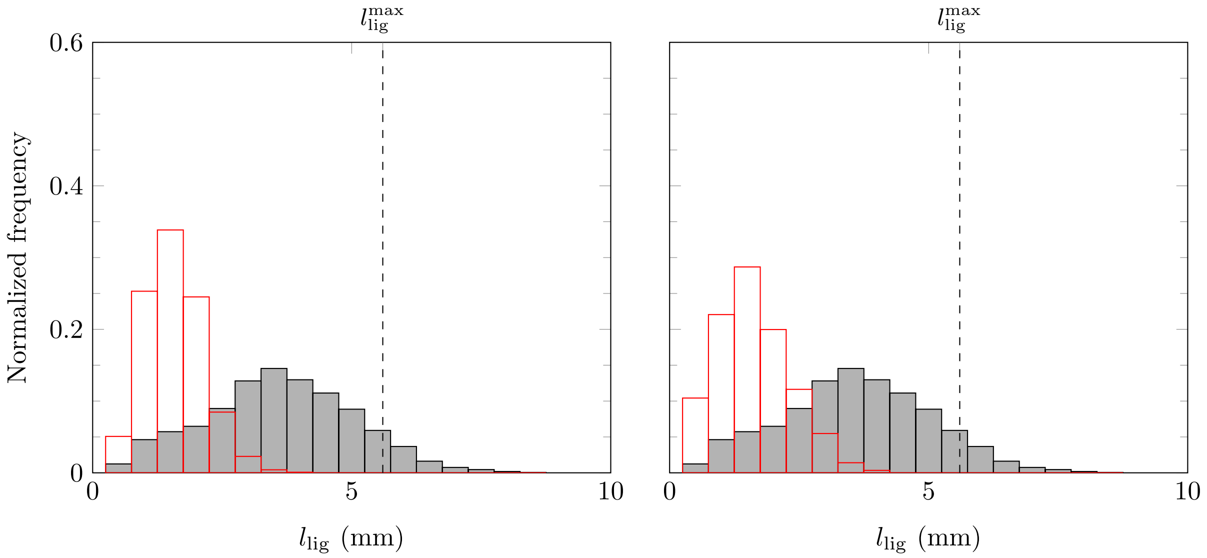

(a) Flat profile (Fp) case

(b) Channel profile (Cp) case

Figure 24: Plots of frequency distributions of the ligament lengths between experiment (■) and simulations (□) for flat profile (Fp) and channel profile (Cp) cases. The maximum measurable ligament length in the computational domain $l_{\text{lig}}^{\text{max}} = 5.6\,\text{mm}$ is marked in the plot using dashed line.

4.3.2. Ligament breakup velocity

As a final quantitative extraction of the atomization characteristics, the velocity of the ligaments w_{lig} at the trailing edge of the pre-filmer plate is computed. The rationale to compute this quantity is to subsequently determine the ligament breakup frequency which can potentially give an idea towards the rate of atomization/breakup. The breakup frequency is a vital quantity in identifying and isolating the study into ligament based breakup mechanism.

To that end, we employ a technique [22] exploiting the displacement of the interface of the 1D contour of the accumulated liquid between adjacent sampled time steps from the simulations (similar to the experimental measurements) to compute the ligament velocity. Such a technique is employed to determine the ligament breakup velocity from the simulations in order to have a consistent comparison with the experimental data. The procedure to obtain the velocity of the identified ligaments (i.e., all filtered maxima from the 1D interface contour) is as follows. Due to the interface wrinkling, it is challenging to identify a single point on the 1D interface contour (see Figure 22d) using which ligament velocity between adjacent time steps can be computed (see Figure 25). Moreover, the ligaments are stripped throughout the width of the pre-filmer plate, thus, choosing one point for the computation of ligament velocity would not be a complete description and not be representative of the ligament breakup velocity. Therefore, in order to overcome this challenge, a simplified calculation is performed in which we determine the displacement of the 1D interface contour by finding the most remote point (along the downstream $z-$direction) $z_{\max}$ for each point in the spanwise $y-$direction between the adjacent time steps t^n and t^{n+1}. The ligament velocity along the streamwise direction is then computed as

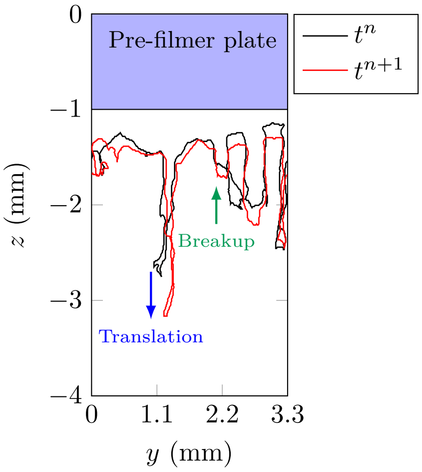

Figure 25: Displacement of interface.

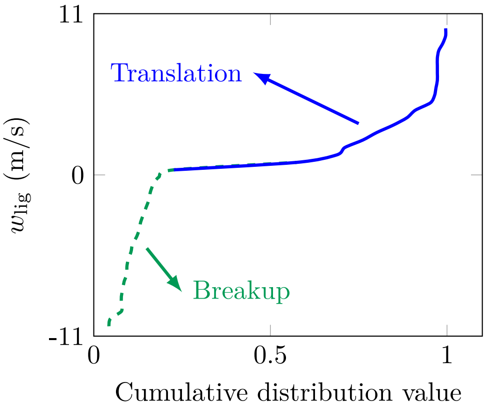

Figure 26: Cumulative distribution of w_{lig}.

$$w_{\text{lig}_j} = \frac{z_{\max,y_j}(t^{n+1}) - z_{\max,y_j}(t^n)}{t^{n+1} - t^n} \quad \forall\ j = 1, 2 \ldots N_y, \tag{17}$$

where N_y is the total number of grid points along the $y-$direction in the computational domain in the simulations. Now, the obvious question is, which velocity on the point y_j need to be considered as the ligament velocity? To answer that question, we compute a cumulative frequency distribution of the computed ligament velocity shown in Figure 26 for a consecutive sampled time step pair (t_1, t_2). The negative velocities (shown by green dashed line in this figure) represent the breakup of the ligaments while the positive velocities (shown by blue solid line) represent the translation/advection of the ligaments. The study by Warncke et al. [22] had taken the 90%-quantile from this distribution as the representative velocity of the ligaments. However, in this work, the ligament velocities are computed for three different quantiles – 90%-, 95%-, and 99.75%-quantiles. The rationale behind this approach is to demonstrate the dependence of the ligament velocity on the selection of quantile. For the sake of the simplicity in notation, each quantile is represented by q where $q = 90, 95, 99.75$ for the remainder of this subsection. The mean value of this quantile velocity is considered to be the ligament breakup velocity computed as

$$w_{\text{lig}}^{\text{breakup},q} = \frac{\sum\limits_{i=1}^{N} w_{\text{lig}}^{q}}{N}, \tag{18}$$

where N is the number of sampled consecutive time step pairs from the simulations and $q = 90, 95, 99.75$ is not an exponent.

Based on this expression, the ligament breakup velocity $w_{\text{lig}}^{\text{breakup},90}$ along the streamwise direction from the simulations are determined to be 2.48 m/s for the Fp case and 2.16 m/s for Cp case. Similarly, the computation of the ligament breakup velocity for 95%-quantile $w_{\text{lig}}^{\text{breakup},95}$ yield 4.06 m/s for the Fp case and 3.06 m/s for Cp case. Finally, the computation using the 99.75%-quantile yield 17.72 m/s for the Fp case and 9.00 m/s for Cp case. The ligament breakup/deformation velocity from the experiments is determined to be 15.7 m/s [22]. A number based frequency distribution of the ligament velocities w_{lig}^{90}, w_{lig}^{95}, $w_{\text{lig}}^{99.75}$ are presented in Figures 27 to 29 shedding light on the spread of the ligament velocity. From this plot, it can be seen that the simulation results are under-predicting the experimental data for the ligament velocities computed using 90% and 95%-quantiles and having good agreement for the 99.75%-quantile. The under-prediction in the case of the former two quantiles point to the requirement of finer computational mesh and time sampling of the data. A finer mesh would be helpful in preventing numerically induced ligament breakup thereby sustaining the long ligaments for longer simulation time. Moreover, these observed high number based frequencies for small ligament velocity values could be attributed to the large sampling time between consecutive sampled time instants from the simulations. In this work, we have sampled every 35 µs which is chosen based on the existing available computational resources [67]. It is expected that within this sampling time, numerous breakup events occur leading to changes in the shape of the accumulated liquid occurring at the trailing edge of the pre-filmer plate affecting the ligament velocity computation.

Finally, when comparing the profiles of the histograms for the Fp and Cp cases, we find that the 90%-quantile plots are not very different from each other except that the Cp case (Figure 27b) is predicting relatively larger number of ligaments having lower velocities. The same observation can be made for the 95%-quantile plot comparing the Fp and Cp cases. However, when observing the 99.75%-quantile plots (c.f. Figure 29b), we find that the ligament velocities from the flat velocity inlet profile is agreeing relatively well with experiments than that with the channel profile case. In fact, both the inlet velocity profile cases are predicting ligament velocities beyond the measurement range of the experimental data indicating the potentiality of the simulations in exploring the altitude relight operating condition for this atomization case.

The global liquid sheet oscillation frequency is challenging to be determined as there is no continuous flapping sheet behind the trailing edge of the pre-filmer plate. Alternatively, mean ligament breakup frequency [22] could be loosely coupled with the frequency of the flapping of the liquid sheet. This breakup frequency (f^{breakup}) is computed as a measure of the time distance between consecutive events of atomization using the following expression

$$f^{\text{breakup}} = \frac{L_{\text{lig}}^{\text{breakup}}}{w_{\text{lig}}^{\text{breakup},q}}. \tag{19}$$

This frequency is computed for each quantiled ligament velocity in the simulations and is determined to be 1878.79 Hz for the Fp case and 1393.56 Hz for the Cp case for 90%-quantiled ligament velocity, 3075.76 Hz for the Fp case and 1974.19 Hz for the Cp case for 95%-quantiled ligament velocity, and 13,424.24 Hz for the Fp case and 5806.45 Hz for the Cp case for 99.75%-quantiled ligament velocity while the value from the experiments [22] is determined as 4906.25 Hz. It can be seen that the simulation results are under-predicting the experimental value for the 90%- and 95% quantiles while over-predicting for the 99.75%-quantile value. Nevertheless, the breakup frequency obtained from the simulation are of the same order of magnitude as the experiments except for the 99.75%-quantiled ligament velocity for the Fp case. Finally, the results presented in this subsection regarding the near-field data of the ligaments are summarized in Table 5. As can be

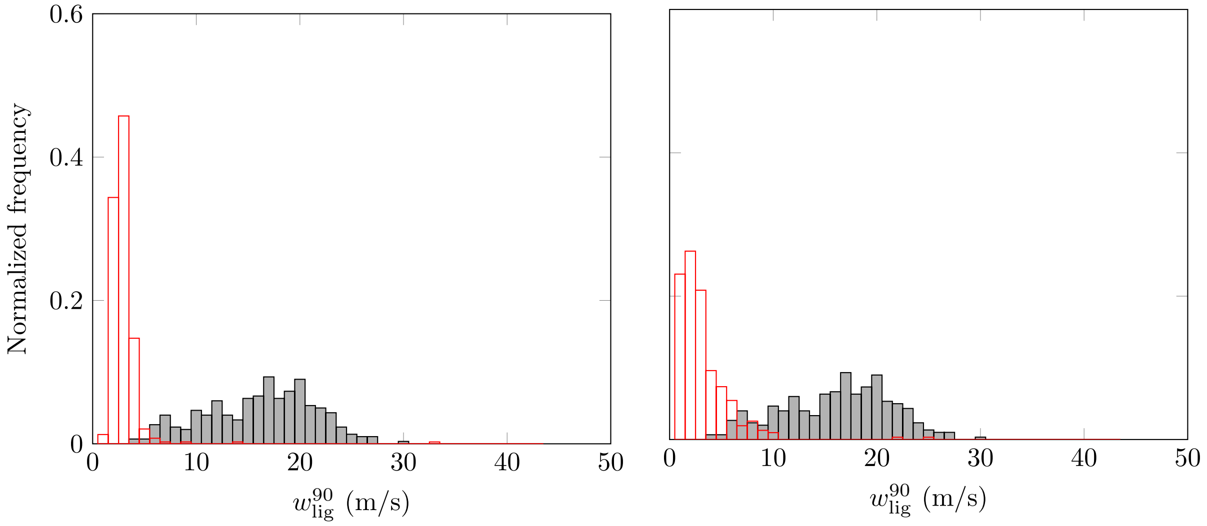

(a) Flat profile (Fp) case

(b) Channel profile (Cp) case

Figure 27: Plots of frequency distribution of the ligament velocity from experiment (▨) and simulations (□) for 90%-quantile ligament velocity.

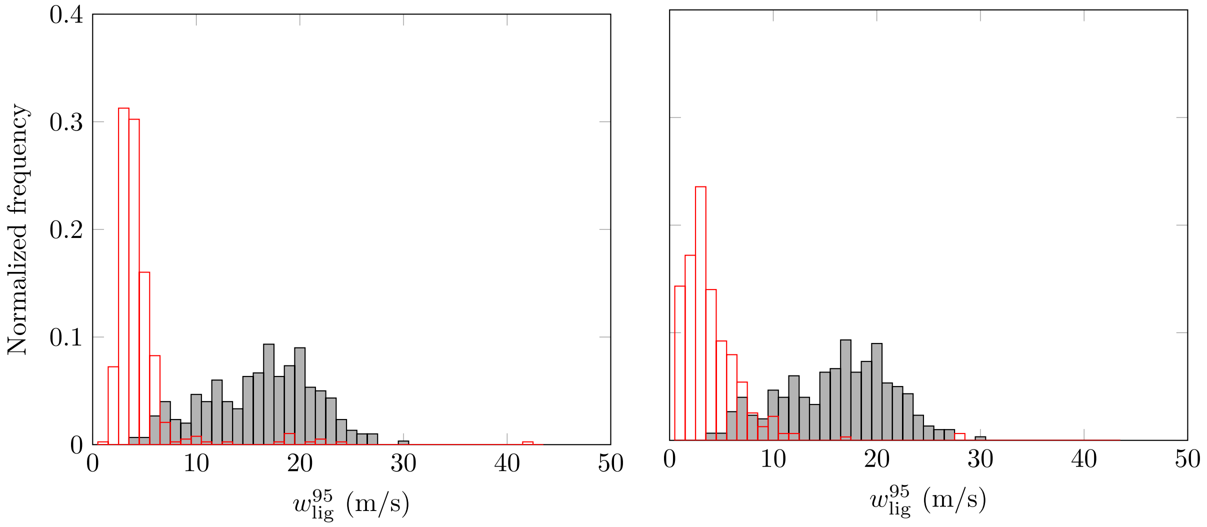

(a) Flat profile (Fp) case

(b) Channel profile (Cp) case

Figure 28: Plots of frequency distribution of the ligament velocity from experiment (▨) and simulations (□) for 95%-quantile ligament velocity.

observed from this table, the order of magnitude change with the sampling is higher for the Fp case than that for the Cp case. In fact, the main difference arises especially for the 99.75% sampling for the ligament velocity computation. The increase in the percentage in sampling (i.e., 90%, 95%, and 99.85%) physically correlates to the increase in tendency to choose the ligament with highest velocity for each sampled time step (c.f. Figure 25) as the representative velocity for it. Since the Fp has the sharp velocity gradient it causes the ligaments to attain very high velocity upon atomization which is not occurring in the case of Cp due to the smooth transition between the liquid and gas phase velocities. Hence, we see that the jump in the order of magnitude observed with increase in sampling for the Fp case to be higher than that for the

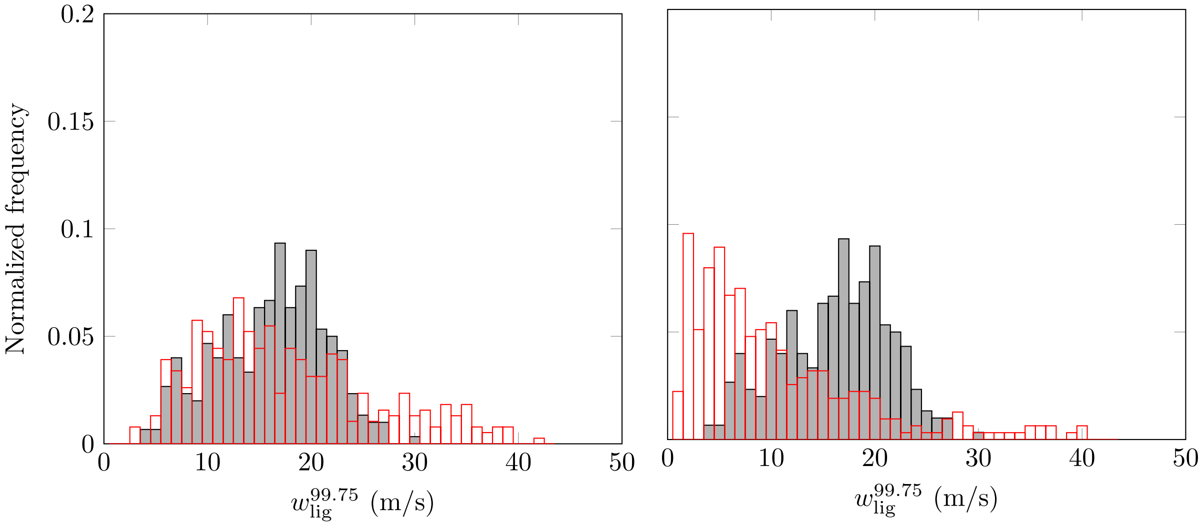

(a) Flat profile (Fp) case

(b) Channel profile (Cp) case

Figure 29: Plots of frequency distribution of the ligament velocity from experiment (▨) and simulations (□) for 99.75%-quantile ligament velocity.

Cp case.

Table 5: Summary of ligament characteristics from the experiments and simulations.

Quantities	**Experiments** [22]	**Simulations**					
		Flat profile (Fp)			Channel profile (Cp)		
		$q = 90$	$q = 95$	$q = 99.75$	$q = 90$	$q = 95$	$q = 99.75$
Breakup velocity ($w_{\text{lig}}^{\text{breakup},q}$) [m/s]	15.7	2.48	4.06	17.72	2.87	3.69	10.36
Breakup length ($L_{\text{lig}}^{\text{breakup}}$) [mm]	3.20	1.32			1.38		
Breakup frequency (f^{breakup}) [Hz]	4906.25	1878.79	3075.76	13424.24	2079.71	2673.91	7507.24

Finally, in order to summarize the results presented in this paper, we have tabulated the inferences (in comparison to the experimental data) obtained for each quantitative results obtained for the Fp and Cp simulation cases in Table 6. As seen in this table, the Cp inlet velocity profile case corresponding to a linear profile for liquid phase and turbulent channel flow profile for the gas phase is relatively having better atomization characteristics than Fp case. This leads us to the conclusion that the Cp case closely approximates the real inlet velocity profile from the experimental investigation.

5. Conclusions

Results from the detailed numerical simulations of planar pre-filming airblast atomization have been presented. The simulations have been performed for an aircraft altitude relight operating condition using hybrid moment of fluid–level set (HyMOFLS) method of liquid/gas interface reconstruction within the

Table 6: Relative comparison between flat profile (Fp) and channel profile (Cp) cases for prediction of various physical quantities with experimental data.

Physical quantity	Criteria	Flat profile (Fp)	Channel profile (Cp)
Drop size distribution (DSD)	Small drops	Under-prediction	Under-prediction
	Large Drops	Over-prediction	Over-prediction
Drop velocity distribution (DVD)	–	Good agreement	Good agreement
Sauter Mean Diameter (SMD)	–	Satisfactory agreement	Good agreement
Ligament lengths		Same order of magnitude	Same order of magnitude
Ligament velocities	90%-quantile	Under-prediction	Under-prediction
	95%-quantile	Under-prediction	Under-prediction
	99.75%-quantile	Excellent agreement	Excellent agreement

context of multiphase flows. The geometry of the annular atomizer is reduced to a planar pre-filming configuration with the rationale of direct and consistent comparison of the simulation results with the experimental data and easy generation of inlet boundary conditions in the simulations. Two different inlet velocity profiles (flat profile and channel flow profile) have been used in the simulations to investigate their influence on the characteristics and quality of the atomization. The turbulence in the simulations have been generated in the gas phase using synthetic turbulence method.

The interface visualizations realized from the simulations show that the overall atomization process comprises of the high speed air destabilizing the liquid fuel film/sheet injected on the solid pre-filmer plate resulting in accumulation of the liquid at the trailing edge of the plate. This accumulated liquid either forms bag-like structure which then breaks up into droplets or forms ligaments at the edge of the plate which disintegrates into droplets. The bag/sheet breakup mechanism and ligament breakup mechanism have been observed to be the two predominant breakup mechanisms driving the airblast atomization for this configuration. The former breakup mechanism often produces droplets that are of the size of the thickness of the sheet while the latter mechanism produces droplets of the size of the ligament diameter which is usually larger than the bag/sheet thickness. Such a combination of breakup mechanism has been found to be consistent with the experimental observations. The quantitative comparison of the drop size distribution (DSD) and drop velocity distribution (DVD) between simulations and experiments showed that the simulation results are of the same magnitude as that of the experimental results however, under-predicting quantitatively. Moreover, the Sauter Mean Diameter (SMD) determined from the simulations are having excellent agreement with the experiments. As a novel analysis, the near-field atomization characteristics pertaining to the liquid ligaments have been extracted from the simulations. The attributes of the ligaments extracted include their breakup length and associated breakup velocity. The ligament lengths from the simulations have been observed to be of the same order of magnitude as that of the experiments although their frequency distributions are under-predicted. The ligament velocity computed from the simulations have been observed to be under-predicting the experimental data although of the same order of magnitude as the experimental data. This could be attributed to the long measurement time and the large domain size in the experiments compared to the simulations. In summary, the ability to simulate such a high shear atomization mechanism by the HyMOFLS method has been demonstrated with the results from simulations and experiments being in the same order of magnitude agreement for the airblast atomization phenomenon.

One of the many directions to improve the results from the simulations is through adaptive mesh refinement (AMR) which would be beneficial to capture the local atomization events and capture the breakup physics through local mesh refinement. New developments are planned towards implementation of AMR strategy to analyze the physics of the breakup and instability waves formed on the liquid sheet.

Acknowledgements

The funding for this project from the European Union's Horizon 2020 research and innovation programme under the Marie Skłodowska-Curie grant agreement N° 675676 is gratefully acknowledged. The authors would like to thank Prof. Dr. Jean-Bernard Blaisot for graciously sharing the algorithm of finding the 1D interface contour. The authors wish to thank Dr. Rainer Koch and his group at Institut für Thermische Strömungsmaschinen in Karlsruher Institut für Technologie (KIT), Germany for graciously sharing their experimental data. Anirudh Asuri Mukundan express gratitude to Dr. Fabien Thiesset for blender image rendering tutorial and beginner scripts and to Dr. Ruud Eggels and Dr. Max Staufer for many fruitful discussions. The computing time at CRIANN (Centre Régional Informatique et d'Applications Numériques de Normandie) under the scientific project No. 2003008 and at GENCI-[TGCC/CINES/IDRIS] (Grant2019-2613) are also gratefully acknowledged.

References

[1] Boeing Current Market Outlook 2019–2038, Technical Report, Boeing, 2019.

[2] Airbus Global Market Forecast 2019–2038, Technical Report, Airbus, 2019.

[3] Flightpath 2050 Europe's Vision for Aviation, Technical Report, European Commission, 2011. `arXiv:https://ec.europa.eu/transport/sites/default/files/modes/air/doc/flightpath2050.pdf`.

[4] ACARE: Aeronautics and air transport: beyond vision 2020(towards 2050)., Technical Report, The Advisory Council for Aeronautics Researchin Europe - Strategy Review Group, European Commission, 2010. `arXiv:https://pq-ue.ani.pt/brochuras/h2020/transportes/a-background-document-from-acare.pdf`.

[5] ACARE Time for Change, Technical Report, Advisory Council for Aeronautics Research in Europe (ACARE), 2020.

[6] Y. Liu, X. Sun, V. Sethi, D. Nalianda, Y.-G. Li, L. Wang, Review of modern low emissions combustion technologies for aero gas turbine engines, Progress in Aerospace Sciences 94 (2017) 12–45. URL: `https://doi.org/10.1016/j.paerosci.2017.08.001`. doi:`10.1016/j.paerosci.2017.08.001`.

[7] GE9X's New TAPS Combustor to Maintain Its Cool Under Fire, 2014. URL: `https://www.geaviation.com/press-release/ge90-engine-family/ge9xs-new-taps-combustor-maintain-its-cool-under-fire`.

[8] V. McDonell, Lean Combustion, second edition ed., Academic Press, 2016, pp. 147–201. URL: `https://doi.org/10.1016/B978-0-12-804557-2.00005-5`. doi:`10.1016/B978-0-12-804557-2.00005-5`.

[9] S. Gepperth, A. Müller, R. Koch, H.-J. Bauer, Ligament and droplet characteristics in prefilming airblast atomization, in: Proceedings of the ICLASS, 12th Triennial International Conference on Liquid Atomization and Spray Systems, September 2-6, Heidelberg, Germany, 2012.

[10] A. H. Lefebvre, D. Miller, The development of an Air Blast Atomizer for gas turbine application, Technical Report CoA Report AERO No. 193, The College of Aeronautics Cranfield, 1966.

[11] J. C. Lasheras, E. Villermaux, E. J. Hopfinger, Break-up and atomization of a round water jet by a high-speed annular air jet, Journal of Fluid Mechanics 357 (1998) 351–379. URL: `https://doi.org/10.1017/S0022112097008070`. doi:`10.1017/S0022112097008070`.

[12] E. Villermaux, Mixing and spray formation in coaxial jets, Journal of Propulsion and Power 14 (1998) 807–817. doi:`10.2514/2.5344`.

[13] P. Marmottant, E. Villermaux, On spray formation, Journal of Fluid Mechanics 498 (2004) 73–111. URL: `https://doi.org/10.1017/S0022112003006529`. doi:`10.1017/S0022112003006529`.

[14] R. Chiodi, G. Agbaglah, O. Desjardins, Validation and analysis of air-blast atomization simulations, in: Proceedings of the ILASS Americas, 28th Annual Conference on Liquid Atomization and Spray Systems, May 15-18, Dearborn, MI, USA, 2016.

[15] R. Chiodi, O. Desjardins, A numerical parametric study on the air-blast atomization of a planar liquid layer, in: Proceedings of the 55th AIAA Aerospace Sciences Meeting, January 9-13, Grapvine, TX, USA, 2017. URL: `https://doi.org/10.2514/6.2017-1702`. doi:`10.2514/6.2017-1702`.

[16] R. Chiodi, O. Desjardins, An exploration of initial destabilization during air-blast atomization using 3d simulations, in: Proceedings of the ILASS Americas 29th Annual Conference on Liquid Atomization and Spray Systems, May 15-18, Atlanta, GA, USA, 2017.

[17] M. Owkes, O. Desjardins, A mass and momentum conserving unsplit semi-Lagrangian framework for simulating multiphase flows, Journal of Computational Physics 332 (2017) 21–46. URL: `https://doi.org/10.1016/j.jcp.2016.11.046`. doi:`10.1016/j.jcp.2016.11.046`.

[18] R. Chiodi, O. Desjardins, A reformulation of the conservative level set reinitialization equation for accurate and robust simulation of complex multiphase flows, Journal of Computational Physics 343 (2017) 186–200. URL: `https://doi.org/10.1016/j.jcp.2017.04.053`. doi:`10.1016/j.jcp.2017.04.053`.

[19] U. C. Bhayaraju, C. Hassa, Planar liquid sheet breakup of prefilming and nonprefilming atomizers at elevated pressures, Atomization and Sprays 19 (2009) 1147–1169. doi:`10.1615/AtomizSpr.v19.i12.50`.

[20] A. K. Jasuja, Behaviour of aero-engine airblast sprays in practical environment, in: Proceedings of the ICLASS, 10th Triennial International Conference on Liquid Atomization and Spray Systems, Aug 27-Sept 1, Kyoto, Japan, 2006.

[21] S. Holz, G. Chaussonnet, S. Gepperth, R. Koch, H.-J. Bauer, Comparison of the Primary Atomization Model PAMELA with Drop Size Distributions of an Industrial Prefilming Airblast Nozzle, in: Proceedings of the ILASS Europe, 27th Annual Conference on Liquid Atomization and Spray Systems, September 4-7, Brighton, UK, 2016.

[22] K. Warncke, S. Gepperth, B. Sauer, A. Sadiki, J. Janicka, R. Koch, H.-J. Bauer, Experimental and numerical investigation of the primary breakup of an airblasted liquid sheet, International Journal of Multiphase Flow 91 (2017) 208–224. URL: `http://dx.doi.org/10.1016/j.ijmultiphaseflow.2016.12.010`. doi:`10.1016/j.ijmultiphaseflow.2016.12.010`.

[23] C. Bilger, R. S. Cant, From high-fidelity numerical simulations of a liquid-film atomization to a regime classification, Atomization and Sprays 28 (2018) 65–89. doi:`10.1615/AtomizSpr.2018025001`.

[24] C. Bilger, Numerical Investigation of Liquid Film Dynamics and Atomisation in Jet Engine Fuel Injectors, Ph.D. thesis, University of Cambridge, 2018. URL: `https://doi.org/10.17863/CAM.21305`. doi:`10.17863/CAM.21305`.

[25] G. Chaussonnet, T. Laroche, C. Lieber, S. Holz, R. Koch, H.-J. Bauer, Investigation of the liquid accumulation characteristics in planar prefilming airblast atomization, in: Proceedings of the ICLASS, 14th Triennial International Conference on Liquid Atomization and Spray Systems, July 22-26, Chicago, IL, USA, 2018.

[26] A. H. Lefebvre, Airblast atomization, Progress in Energy and Combustion Science 6 (1980) 233–261. URL: `https://doi.org/10.1016/0360-1285(80)90017-9`. doi:`10.1016/0360-1285(80)90017-9`.

[27] M. M. Aigner, S. Wittig, Swirl and counterswirl effects in prefilming airblast atomizers, Journal of Engineering for Gas Turbines and Power 110 (1988) 105–110. URL: `https://doi.org/10.1115/1.3240072`. doi:`10.1115/1.3240072`.

[28] U. C. Bhayaraju, F. Giuliani, C. Hassa, Planar liquid sheet breakup of pre- and nonprefilming airblast atomisers at elevated ambiant air pressures, in: Proceedings of the ILASS Europe, 20th Annual Conference on Liquid Atomization and Spray Systems, September 5-7, Orléans, France, 2005.

[29] J. E. Beck, A. H. Lefebvre, T. R. Koblish, Airblast atomization at conditions of low air velocity, Journal of Propulsion and Power 7 (1991) 207–212. URL: `https://doi.org/10.2514/3.23313`. doi:`10.2514/3.23313`.

[30] G. Chaussonnet, S. Gepperth, S. Holz, R. Koch, H.-J. Bauer, Influence of the ambient pressure on the liquid accumulation and on the primary spray in prefilming airblast atomization, International Journal of Multiphase Flow 125 (2020) 103229. URL: `https://doi.org/10.1016/j.ijmultiphaseflow.2020.103229`. doi:`10.1016/j.ijmultiphaseflow.2020.103229`.

[31] D. Fuster, J.-P. Matas, S. Marty, S. Popinet, J. Hoepffner, A. Cartellier, S. Zaleski, Instability regimes in the primary breakup region of planar coflowing sheets, Journal of Fluid Mechanics 736 (2013) 150–176. URL: `https://doi.org/10.1017/jfm.2013.536`. doi:`10.1017/jfm.2013.536`.

[32] G. Agbaglah, R. Chiodi, O. Desjardins, Numerical simulation of the initial destabilization of an air-blasted liquid layer, Journal of Fluid Mechanics 812 (2017) 1024–1038. URL: `https://doi.org/10.1017/jfm.2016.835`. doi:`10.1017/jfm.2016.835`.

[33] T. Inamura, M. Shirota, M. Tsushima, M. Kato, Spray characteristics of prefilming type of airblast atomizer, in: Proceedings of the ICLASS, 12th Triennial International Conference on Liquid Atomization and Spray Systems, September 2-6, Heildelberg, Germany, 2012.

[34] B. Déjan, P. Berthoumieu, P. Gajan, Experimental study on the influence of liquid and air boundary conditions on a planar air-blasted liquid sheet, part i: Liquid and air thicknesses, International Journal of Multiphase Flow 79 (2016) 202–213. URL: `https://doi.org/10.1016/j.ijmultiphaseflow.2015.09.002`. doi:`10.1016/j.ijmultiphaseflow.2015.09.002`.

[35] B. Déjan, P. Berthoumieu, P. Gajan, Experimental study on the influence of liquid and air boundary conditions on a planar air-blasted liquid sheet, part ii: prefilming zone length, International Journal of Multiphase Flow 79 (2016) 214–224. URL: `https://doi.org/10.1016/j.ijmultiphaseflow.2015.09.001`. doi:`10.1016/j.ijmultiphaseflow.2015.09.001`.

[36] G. Chaussonnet, E. Riber, O. Vermorel, B. Cuenot, S. Gepperth, R. Koch, Large eddy simulation of a prefilming airblast atomizer, in: Proceedings of the ILASS Europe, 25th Annual Conference on Liquid Atomization and Spray Systems, September 1-4, Chania, Greece, 2013.

[37] G. Chaussonnet, O. Vermorel, E. Riber, B. Cuenot, A new phenomenological model to predict drop size distribution in large-eddy simulations of airblast atomizers, International Journal of Multiphase Flow 80 (2016) 29–42. URL: `https://doi.org/10.1016/j.ijmultiphaseflow.2015.10.014`. doi:`10.1016/j.ijmultiphaseflow.2015.10.014`.

[38] B. Sauer, A. Sadiki, J. Janicka, Numerical analysis of the primary breakup applying the embedded dns approach to a generic prefilming airblast atomizer, The Journal of Computational Multiphase Flows 6 (2014) 179–192. URL: `https://doi.org/10.1260/1757-482X.6.3.179`. doi:`10.1260/1757-482X.6.3.179`.

[39] B. Sauer, A. Sadiki, J. Janicka, Embedded dns concept for simulating the primary breakup of an airblast atomizer, Atomization and Sprays 26 (2016) 187–217. URL: `http://dx.doi.org/10.1615/AtomizSpr.2014011019`. doi:`10.1615/AtomizSpr.2014011019`.

[40] B. Sauer, Direct Numerical Simulation of the Primary Breakup of Aircraft Engine Related Two-Phase Flows, Ph.D. thesis, Technische Univesität Darmstadt, 2016.

[41] S. Braun, L. Weith, S. Holz, T. F. Dauch, M. C. Keller, G. Chaussonnet, S. Gepperth, R. Koch, H.-J. Bauer, Numerical prediction of air-assisted primary atomization using smoothed particle hydrodynamics, International Journal of Multiphase Flow (2019).

[42] S. Holz, S. Braun, G. Chaussonnet, R. Koch, H.-J. Bauer, Close Nozzle Spray Characteristics of a Prefilming Airblast Atomizer, Energies 12 (2019) 2835–2856. URL: `https://doi.org/10.3390/en12142835`. doi:`10.3390/en12142835`.

[43] S. Gepperth, D. Guildenbecher, R. Koch, H.-J. Bauer, Pre-filming primary atomization: Experiments and modeling, in: Proceedings of the ILASS Europe, 23rd Annual Conference on Liquid Atomization and Spray Systems, September 6-8, Brno, Czech Republic, 2010.

[44] A. Müller, Experimentelle Untersuchung des Zerstäubungsverhaltens luftgestützter Brennstoffdüsen bei osczillierenden Strömungen, Ph.D. thesis, Institut für Thermische Strömungsmaschinen (ITS), Karlsruhe Institut für Technologie, 2015.

[45] A. Müller, R. Koch, H.-J. Bauer, M. Hehle, O. Schäfer, Performance of prefilming airblast atomizers in unsteady flow

conditions, in: Proceedings of the ASME Turbo Expo 2006: Power for Land, Sea and Air, May 8-11, Barcelona, Spain, 2006. URL: https://doi.org/10.1115/GT2006-90432. doi:10.1115/GT2006-90432.

[46] R. Kapulla, J. Tuchtenhagen, A. Müller, K. Dullenkopf, H.-J. Bauer, Droplet sizing performance of different shadow sizing codes, Gesellschaft für Laser-Anemometrie GALA, Karlsruhe, Germany (2008).

[47] S. J. Kline, F. A. McClintock, Describing uncertainties in single-sample experiments, Mechanical Engineering 75 (1953) 3–8.

[48] T. Mosbach, R. Sadanandan, W. Meier, R. Eggels, Experimental analysis of altitude relight under realistic conditions using laser and high-speed video techniques, in: Proceedings of the ASME Turbo Expo 2010: Power for Land, Sea, and Air, Volume 2: Combustion, Fuels and Emissions, Parts A and B, June 14–18, Glasgow, UK, volume 2, 2010. doi:10.1115/GT2010-22625.

[49] A. Behrendt, T. Nakamura, T. Tsuda, Combined temperature lidar for measurements in the troposphere, stratosphere, and mesosphere, Applied Optics 43 (2004) 2930–2939. URL: http://doi.org/10.1364/AO.43.002930. doi:10.1364/AO.43.002930.

[50] G. Chaussonnet, T. Dauch, M. Keller, M. Okraschevski, C. Ates, C. Schwitzke, R. Koch, H.-J. Bauer, Progress in the Smoothed Particle Hydrodynamics Method to Simulate and Post-process Numerical Simulations of Annular Airblast Atomizers, Flow, Turbulence and Combustion 105 (2020). URL: https://doi.org/10.1007/s10494-020-00174-6. doi:10.1007/s10494-020-00174-6.

[51] T. Ménard, S. Tanguy, A. Berlemont, Coupling level set/VOF/ghost fluid methods: Validation and application to 3D simulation of the primary break-up of a liquid jet, International Journal of Multiphase Flow 33 (2007) 510–524. URL: https://doi.org/10.1016/j.ijmultiphaseflow.2006.11.001. doi:10.1016/j.ijmultiphaseflow.2006.11.001.

[52] A. Asuri Mukundan, T. Ménard, J. C. Brändle de Motta, A. Berlemont, A 3D Moment of Fluid method for simulating complex turbulent multiphase flows, Computers & Fluids 198 (2020). URL: https://doi.org/10.1016/j.compfluid.2019.104364. doi:10.1016/j.compfluid.2019.104364.

[53] G. Vaudor, T. Ménard, W. Aniszewski, M. Doring, A. Berlemont, A consistent mass and momentum flux computation method for two phase flows. Application to atomization process, Computers & Fluids 152 (2017) 204–216. URL: https://doi.org/10.1016/j.compfluid.2017.04.023. doi:10.1016/j.compfluid.2017.04.023.

[54] B. Duret, G. Luret, J. Réveillon, T. Ménard, A. Berlemont, F.-X. Demoulin, DNS analysis of turbulent mixing in two-phase flows, International Journal of Multiphase Flow 40 (2012) 93–105. URL: https://doi.org/10.1016/j.ijmultiphaseflow.2011.11.014. doi:10.1016/j.ijmultiphaseflow.2011.11.014.

[55] R. Canu, S. Puggelli, M. Essadiki, B. Duret, T. Ménard, M. Massot, J. Réveillon, F. Demoulin, Where does the droplet size distribution come from?, International Journal of Multiphase Flow 107 (2018) 230–245. URL: https://doi.org/10.1016/j.ijmultiphaseflow.2018.06.010. doi:10.1016/j.ijmultiphaseflow.2018.06.010.

[56] V. Chéron, J. C. Brändle de Motta, G. Vaudor, T. Ménard, A. Berlemont, From droplets to particles: Transformation criteria, in: Proceedings of the ILASS Europe, 29th Annual Conference on Liquid Atomization and Spray Systems, September 2-4, Paris, France, 2019.

[57] J. Cousin, T. Ménard, A. Berlemont, S. Grout, Primary breakup simulation of a liquid jet discharged by a low-pressure compound nozzle, Computers & Fluids 63 (2012) 165–173. URL: http://dx.doi.org/10.1016/j.compfluid.2012.04.013. doi:10.1016/j.compfluid.2012.04.013.

[58] B. Duret, J. Réveillon, T. Ménard, F. X. Demoulin, Improving primary atomization modeling through DNS of two-phase flows, International Journal of Multiphase Flow 55 (2013) 130–137. URL: https://doi.org/10.1016/j.ijmultiphaseflow.2013.05.004. doi:10.1016/j.ijmultiphaseflow.2013.05.004.

[59] A. Asuri Mukundan, G. Tretola, T. Ménard, M. Herrmann, S. Navarro-Martinez, K. Vogiatzaki, J. C. Brändle de Motta, A. Berlemont, DNS and LES of primary atomization of turbulent liquid jet injection into a gaseous crossflow environment (2020). URL: https://doi.org/10.1016/j.proci.2020.08.004. doi:10.1016/j.proci.2020.08.004.

[60] M. Sussman, K. M. Smith, M. Y. Hussaini, M. Ohta, R. Zhi-Wei, A sharp interface method for incompressible two-phase flows, Journal of Computational Physics 221 (2007) 469–505. URL: https://doi.org/10.1016/j.jcp.2006.06.020. doi:10.1016/j.jcp.2006.06.020.

[61] R. Fedkiw, T. Aslam, B. Merriman, S. Osher, A Non-oscillatory Eulerian Approach to Interfaces in Multimaterial Flows (the Ghost Fluid Method), Journal of Computational Physics 152 (1999) 457–492. URL: https://doi.org/10.1006/jcph.1999.6236. doi:10.1006/jcph.1999.6236.

[62] S. Tanguy, A. Berlemont, Application of a level set method for simulation of droplet collisions, International Journal of Multiphase Flow 31 (2005) 1015–1035. URL: https://10.1016/j.ijmultiphaseflow.2005.05.010. doi:10.1016/j.ijmultiphaseflow.2005.05.010.

[63] T.-T. Vu, Atomization process of turbulent liquid sheets. Experimental analyses & numerical developments, Ph.D. thesis, Université de Rouen Normandie, 2017. URL: http://www.coria.fr/spip.php?article1105&titre_mot=these.

[64] M. Klein, A. Sadiki, J. Janicka, A digital filter based generation of inflow data for spatially developing direct numerical or large eddy simulations, Journal of Computational Physics 186 (2003) 652–665. URL: https://doi.org/10.1016/S0021-9991(03)00090-1. doi:10.1016/S0021-9991(03)00090-1.

[65] S. B. Pope, Turbulent Flows, Cambridge University Press, 2000.

[66] M. Gorokhovski, M. Herrmann, Modeling primary atomization, Annual Review of Fluid Mechanics 40 (2008) 343–366. URL: https://doi.org/10.1146/annurev.fluid.40.111406.102200. doi:10.1146/annurev.fluid.40.111406.102200.

[67] Utilisation du Cluster Myria, CRIANN Supercomputing Facility, Centre Régional Informatique et d'Applications Numériques de Normandie, 2018. URL: http://www-tech.criann.fr/calcul/tech/myria-doc/guide-util/.

[68] A. Asuri Mukundan, T. Ménard, A. Berlemont, J. C. Brändle de Motta, Coupled Level set moment of fluid method for simulating multiphase flows, in: Proceedings of the ILASS Europe, 29th Annual Conference on Liquid Atomization and

Spray Systems, September 2-4, Paris, France, 2019. URL: `https://hal.archives-ouvertes.fr/hal-02318029/document`.

[69] A. Asuri Mukundan, T. Ménard, J. C. Brändle de Motta, A. Berlemont, A hybrid moment of fluid–level set framework for simulating primary atomization (2021 (Under Revision)).

[70] V. Dyadechko, M. Shashkov, Reconstruction of multi-material interfaces from moment data, Journal of Computational Physics 227 (2008) 5361–5384. URL: `https://doi.org/10.1016/j.jcp.2007.12.029`. doi:`10.1016/j.jcp.2007.12.029`.

[71] M. Jemison, E. Loch, M. Sussman, M. Shashkov, M. Arienti, M. Ohta, Y. Wang, A Coupled Level Set-Moment of Fluid Method for Incompressible Two-Phase Flows, Journal of Scientific Computing 54 (2013) 454–491. URL: `https://doi.org/10.1007/s10915-012-9614-7`. doi:`10.1007/s10915-012-9614-7`.

[72] G. D. Weymouth, D. K.-P. Yue, Conservative Volume-of-Fluid method for free-surface simulations on Cartesian-grids, Journal of Computational Physics 229 (2010) 2853–2865. URL: `https://doi.org/10.1016/j.jcp.2009.12.018`. doi:`10.1016/j.jcp.2009.12.018`.

[73] D. Gueyffier, A. Nadim, R. Scardovelli, S. Zaleski, Volume-of-Fluid Interface Tracking with Smoothed Surface Stress Methods for Three-Dimensional Flows, Journal of Computational Physics 152 (1999) 423–456. URL: `https://doi.org/10.1006/jcph.1998.6168`. doi:`10.1006/jcph.1998.6168`.

[74] M. Sussman, E. G. Puckett, A Coupled Level Set and Volume-of-Fluid Method for Computing 3D and Axisymmetric Incompressible Two-Phase Flows, Journal of Computational Physics 162, (2000) 301–337. URL: `https://doi.org/10.1006/jcph.2000.6537`. doi:`10.1006/jcph.2000.6537`.

[75] A. Asuri Mukundan, Numerical development of Moment of Fluid/Level Set method and Application to liquid jet and sheet atomization, Ph.D. thesis, Université de Rouen Normandie, 2020.

[76] V. G. Fernández, P. Berthoumieu, G. Lavergne, Liquid sheet disintegration at high pressure: An experimental approach, Comptes Rendus Mécanique 337 (2009) 481–491. URL: `https://doi.org/10.1016/j.crme.2009.06.026`. doi:`10.1016/j.crme.2009.06.026`.

[77] M. Behzad, A. Mashayek, N. Ashgriz, A KIVA-based model for liquid jet in crossflow, in: Proceedings of the ILASS Americas, 22nd Annual Conference on Liquid Atomization and Spray Systems, May 16-19, Cincinnati, OH, USA, ILASS2010-112, 2010.

[78] M. Herrmann, A parallel Eulerian interface tracking/Lagrangian point particle multi-scale coupling procedure, Journal of Computational Physics 229 (2010) 745–759.

[79] M. Pilch, C. A. Erdman, Use of breakup time data and velocity history data to predict the maximum size of stable fragments for acceleration-induced breakup of a liquid drop, International Journal of Multiphase Flow 13 (1987) 741–757. URL: `https://doi.org/10.1016/0301-9322(87)90063-2`. doi:`10.1016/0301-9322(87)90063-2`.

[80] A. Asuri Mukundan, T. Ménard, A. Berlemont, J. C. Brändle de Motta, An investigation of characteristics of airblast atomization using 3D DNS for altitude relight conditions, in: 11th U.S. National Combustion Meeting, April 24-27, Pasadena, California, USA, 2019. URL: `https://hal.archives-ouvertes.fr/hal-02092003/document`.

[81] A. Asuri Mukundan, T. Ménard, A. Berlemont, J. C. Brändle de Motta, R. Eggels, Validation and Analysis of 3D DNS of planar pre-filming airblast atomization simulations, in: Proceedings of the ILASS Americas, 30th Annual Conference on Liquid Atomization and Spray Systems, May 12-15, Phoenix, AZ, USA, 2019. URL: `https://hal.archives-ouvertes.fr/hal-02178046/document`.

[82] A. Asuri Mukundan, T. Ménard, A. Berlemont, J. C. Brändle de Motta, A comparative study of DNS of airblast atomization using CLSMOF and CLSVOF methods, in: Proceedings of the ILASS Europe, 29th Annual Conference on Liquid Atomization and Spray Systems, September 2-4, Paris, France, 2019. URL: `https://hal.archives-ouvertes.fr/hal-02318020/document`.

[83] N. Fdida, J.-B. Blaisot, Morphological characterization of droplets. application to atomization of sprays, in: ISFV13-13th International Symposium on Flow Visualization, FLUVISU12 - 12th French Congress on Visualization in Fluid Mechanics July 1-4, Nice, France, 2008.

[84] J.-B. Blaisot, Analysis of backlight images for spray measurement: how to accurately identify the liquid-gas interface in images, in: Proceedings of the ICLASS, 14th Triennial International Conference on Liquid Atomization and Spray Systems, July 22-26, Chicago, IL, USA, 2018.